A Finite Strain Plastic-damage Model for High Velocity Impacts using Combined Viscosity and Gradient Localization Limiters: Part II – Numerical Aspects and Simulations

GEORGE Z. VOYIADJIS* AND RASHID K. ABU AL-RUB
Department of Civil and Environmental Engineering
Louisiana State University, Baton Rouge, LA 70803, USA

ABSTRACT: In this companion article, we present within the finite element context the numerical algorithms for the integration of the thermodynamically consistent formulation of geometrically nonlinear gradient-enhanced viscoinelasticity derived in the first part of the article. The proposed unified integration algorithms are extensions of the classical rate-independent return mapping algorithms to the rate-dependent problems. An operator split structure is used consisting of a trial state followed by the return map by imposing the generalized viscoplastic and visco-damage consistency conditions simultaneously. Furthermore, a trivially incrementally objective integration scheme is established for the rate constitutive relations. The proposed finite deformation scheme is based on hypoelastic stress–strain representations and the proposed elastic predictor and coupled viscoplastic–viscodamage corrector algorithm allows for the total uncoupling of geometrical and material nonlinearities. A simple and direct computational algorithm is also used for calculation of the higher-order gradients. This algorithm can be implemented in the existing finite element codes without numerous modifications as compared to the current numerical approaches for integrating gradient-dependent models. The nonlinear algebraic system of equations is solved by consistent linearization and the Newton–Raphson iteration. The proposed model is implemented in the explicit finite element code ABAQUS via the user subroutine VUMAT. Model capabilities are preliminarily illustrated for the dynamic localization of inelastic flow in adiabatic shear bands and the perforation of a 12 mm thick Weldox 460E steel plates by deformable blunt projectiles at various impact speeds. The simulated shear band results well illustrated the potential of the proposed model in dealing with the well-known mesh sensitivity problem. Consequently, the introduced implicit and explicit

*Author to whom correspondence should be addressed. E-mail: Voyiadjis@eng.lsu.edu

1056-7895/06/04 0335–39 $10.00/0 DOI: 10.1177/1056789506058047

length-scale measures are able to predict size effects in localization failures. Moreover, good agreement is obtained between the numerical simulations and experimental results of the perforation problem.

KEY WORDS: finite element method, adiabatic shear bands, perforation, mesh dependence, material length-scales.

INTRODUCTION

Experimental observations of the inelastic behavior of various materials reveal the existence of localization phenomenon. This phenomenon is observed on a wide class of engineering materials including metals, concrete, rock, and soil, which is a characteristic feature of the inelastic deformations. Strain localization is a notion describing a deformation mode, in which the whole deformation of a material structure occurs in one or more narrow bands, while the rest of the structure usually exhibits unloading. The width and direction of localization bands depend on the material parameters, geometry, boundary conditions, loading distribution, and loading rate.

Owing to the lack of classical local continuum formulation to produce physically meaningful and numerically converging results within strain localization computations, a thermodynamically motivated coupled plasticity-damage formulation is presented in the companion article of the first part of this study for rate- and temperature-dependent problems. This model uses combined viscosity and nonlocal gradient localization limiters to regularize the dynamic strain localization problems. The enhanced nonlocal gradient-dependent theory formulates a constitutive framework on the continuum level that is used to bridge the gap between micromechanical theories and classical (local) continuum theories. They are successful in explaining the size effects encountered at the micron scale and in preserving the well-posedeness of the (initial) boundary value problem governing the solution of material instability triggering strain localization. Moreover, viscosity (rate dependency) allows the spatial difference operator in the governing equations to retain its ellipticity and the initial boundary value problem is well-posed. This is due to the incorporation of either explicit (via nonlocal theory) or implicit (via viscosity) intrinsic material length-scale parameter in the constitutive description.

In the first part of this study, a general theoretical framework for the analysis of heterogeneous media that assesses a strong coupling between rate-dependent plasticity and anisotropic rate-dependent damage is presented for high velocity impact related problems. This framework is developed based on thermodynamic laws, nonlinear continuum mechanics,

and nonlocal gradient-dependent theory. The proposed formulation includes hypoelasto-thermo-viscoplasticity with anisotropic thermovisco-damage; a dynamic yield criterion; a dynamic damage growth criterion; non-associated flow rules; thermal softening; nonlinear strain hardening; strain-rate hardening; strain hardening gradients; strain-rate hardening gradients; and an equation of state. The idea of bridging length-scales is made more general and complete by introducing spatial higher-order gradients in the temporal evolution equations of the internal state variables that describe hardening in coupled viscoplasticity and viscodamage models. The model is mainly developed to regularize the ill-posedness caused by strain-softening material behavior and to incorporate the size effect (size and spacing of microdefects) in material behavior for high velocity impact damage related problems.

In this part of the study, we are concerned about the numerical implementation and verification of the highly nonlinear constitutive equations developed in the first part of this article. The development of computational algorithms that are consistent with the proposed theoretical formulation is given in detail in this article. Also, the problem of numerically integrating the constitutive equations in the context of the finite element method is addressed. The standard return mapping algorithms of rate-independent problems are extended to rate-dependent problems. Moreover, since the numerical implementation of the nonlocal gradient-dependent constitutive equations is not a direct task, because of the higher order of the governing equations, a direct and simple computational algorithm for the gradient approach is utilized. This algorithm can be implemented in the existing finite element codes without numerous modifications as compared to current numerical approaches for gradient-enhanced models (see e.g., de Borst and Mühlhaus, 1992; de Borst et al., 1993; Pamin 1994; de Borst and Pamin, 1996; de Borst et al., 1999; and the references quoted therein).

Furthermore, a trivially incrementally objective integration scheme is established for the rate constitutive relations. The proposed elastic predictor and coupled viscoplastic–viscodamage corrector algorithm allows for total uncoupling of geometrical and material nonlinearities. The nonlinear algebraic system of equations is solved by consistent linearization and the Newton–Raphson iteration. The proposed model is implemented in the explicit finite element code ABAQUS (2003) via the user subroutine VUMAT. We present complete details of the implementation of the proposed novel numerical treatment of the problem.

Model capabilities are preliminarily illustrated for the dynamic localization of inelastic flow in adiabatic shear bands and the perforation of 12 mm thick Weldox 460E steel plates by deformable blunt projectiles at various impact speeds.

The numerical integration of the constitutive model developed in Part I of this article is given in the next section along with the descretized form of the equations. In addition, the formal steps involved in the numerical implementation of the model within the framework of the finite element method are considered. Two numerical examples of the formation of adiabatic shear bands are presented and the problem of a projectile penetrating a steel target is simulated. Conclusions are also presented at the end.

NUMERICAL ASPECTS

In this section, the numerical integration of the nonlocal geometrically nonlinear thermoviscoinelastic model developed in Part I of this work are developed. Table 1 summarizes the key ingredients of the model. The subsection on 'General Formulation' presents the equations of motion. The subsequent subsection describes in detail the return mapping algorithm considered in the integration of the proposed nonlocal constitutive model. The return mapping algorithm is based on the extension of the classical predictor–corrector structure of the rate-independent problems to rate-dependent ones. An operator split structure is developed consisting of a trial state followed by the return map by imposing the generalized viscoplastic and viscodamage consistency conditions simultaneously. Furthermore, a trivially incrementally objective integration scheme is established for the rate constitutive relations. The proposed finite deformation scheme is based on hypoelastic stress–strain representations and the proposed elastic predictor and coupled viscoplastic–viscodamage corrector algorithm allows for total uncoupling of geometrical and material nonlinearities. In addition, a simple and direct computational algorithm is also used for the calculation of high-order gradients. The nonlinear algebraic system of equations is solved by consistent linearization and the Newton–Raphson iteration. Representative numerical simulations illustrating the performance of the proposed numerical formulation are included in the section on 'Numerical Applications'. Moreover, note that we use here the same notation as in Part I of the companion article, unless specifically stated otherwise.

General Formulation

Let $t_0, t_1, \ldots, t_n, t_{n+1} = t_n + \Delta t, \ldots$ be convenient time instances along the time interval over which the dynamic response of the body is sought. Consider the time step $\Delta t = t_{n+1} - t_n$: at $t = t_n$ where all quantities are

Table 1. Constitutive model.

1. Stress–strain rate relationship in the spatial and damaged configuration

$$\overset{\nabla}{\boldsymbol{\tau}} = \mathbb{C} : \left(\boldsymbol{d} - \boldsymbol{d}^{\mathrm{vp}} - \boldsymbol{d}^{\mathrm{vd}}\right) - \boldsymbol{A} : \overset{\nabla}{\boldsymbol{\phi}} - \boldsymbol{\beta}\dot{T}, \text{ where } \mathbb{C} = \widehat{\boldsymbol{M}}^{-1} : \bar{\mathbb{C}} : \widehat{\boldsymbol{M}}^{-1},$$

$$\widehat{\boldsymbol{M}} = 2\left[\left(1-\hat{\phi}\right)\otimes \mathbf{1} + \mathbf{1}\otimes\left(1-\hat{\phi}\right)\right]^{-1},$$

$$\bar{\mathbb{C}} = K^{\mathrm{e}}\mathbf{1}\otimes\mathbf{1} + 2G^{\mathrm{e}}\boldsymbol{I}^{\mathrm{dev}}, \text{ and } A_{ijkl} = \frac{\partial \widehat{\boldsymbol{M}}^{-1}}{\partial \hat{\phi}} : \widehat{\boldsymbol{M}} : \boldsymbol{\tau} + \mathbb{C} : \widehat{\boldsymbol{M}} : \frac{\partial \widehat{\boldsymbol{M}}^{-1}}{\partial \hat{\phi}} : \mathbb{C}^{-1} : (\boldsymbol{\tau} + \boldsymbol{\beta}\Delta T)$$

2. Nonlocal viscoplasticity condition in the undamaged configuration

$$f = \sqrt{\frac{3}{2}\left(\bar{\boldsymbol{\tau}}' - \bar{\boldsymbol{X}}\right) : \left(\bar{\boldsymbol{\tau}}' - \bar{\boldsymbol{X}}\right)} - \left[\bar{Y}_{\mathrm{yp}} + \bar{R}\right]\left[1 + \left(\eta^{\mathrm{vp}}\dot{\bar{p}}\right)^{1/m_1}\right]\left[1 - \left(\frac{T}{T_{\mathrm{m}}}\right)^{n}\right] \leq 0$$

3. Nonlocal viscodamage condition

$$g = \sqrt{\left(\bar{\boldsymbol{Y}} - \widehat{\boldsymbol{H}}\right) : \left(\bar{\boldsymbol{Y}} - \widehat{\boldsymbol{H}}\right)} - \left[I + \hat{K}\right]\left[1 + \left(\eta^{\mathrm{vd}}\dot{\bar{r}}\right)^{1/m_2}\right]\left[1 - \left(\frac{T}{T_{\mathrm{m}}}\right)^{n}\right] \leq 0$$

4. Flow rules

$$\boldsymbol{d}^{\mathrm{vp}} = \dot{\lambda}^{\mathrm{vp}}\frac{\partial f}{\partial \boldsymbol{\tau}}, \qquad \boldsymbol{d}^{\mathrm{vd}} = \dot{\lambda}^{\mathrm{vd}}\frac{\partial g}{\partial \boldsymbol{\tau}}, \qquad \overset{\nabla}{\boldsymbol{\phi}} = \dot{\lambda}^{\mathrm{vp}}\frac{\partial f}{\partial \boldsymbol{Y}} + \dot{\lambda}^{\mathrm{vd}}\frac{\partial g}{\partial \boldsymbol{Y}}$$

5. Nonlocal plasticity and damage laws

Plasticity

Isotropic hardening $\quad \dot{\bar{R}} = \dot{\bar{R}} + \frac{1}{2}\ell_1^2\nabla^2\dot{\bar{R}}$ with $\dot{\bar{R}} = \dfrac{a_1\dot{\lambda}^{\mathrm{vp}}}{\left(1-\bar{r}\right)^2}\left(1 - k_1\bar{R}\right)$

Kinematic hardening $\quad \overset{\nabla}{\bar{\boldsymbol{X}}} = \overset{\nabla}{\boldsymbol{X}} + \frac{1}{2}\ell_2^2\nabla^2\overset{\nabla}{\boldsymbol{X}}$ with $\overset{\nabla}{X}_{ij} = a_2\dot{\lambda}^{\mathrm{vp}}\widehat{\boldsymbol{M}} : \widehat{\boldsymbol{M}} : \left(\dfrac{\partial f}{\partial \bar{\boldsymbol{\tau}}} - k_2\bar{\boldsymbol{X}}\right)\left(1 - \left(\dfrac{T}{T_{\mathrm{m}}}\right)^{n}\right)$

Damage

Isotropic hardening $\quad \dot{\bar{K}} = \dot{K} + \frac{1}{2}\ell_3^2\nabla^2\dot{K}$ with $\dot{K} = a_3\dot{\lambda}^{\mathrm{vd}}\left(1 - h_1\bar{K}\right)$

Kinematic hardening $\quad \overset{\nabla}{\bar{\boldsymbol{H}}} = \overset{\nabla}{\boldsymbol{H}} + \frac{1}{2}\ell_4^2\nabla^2\overset{\nabla}{\boldsymbol{H}}$ with $\overset{\nabla}{\boldsymbol{H}} = a_4\dot{\lambda}^{\mathrm{vd}}\left(\dfrac{\partial g}{\partial \boldsymbol{Y}} - h_2\bar{\boldsymbol{H}}\right)\left(1 - \left(\dfrac{T}{T_{\mathrm{m}}}\right)^{n}\right)$

Strain energy release rate $\quad \bar{Y} = \dfrac{1+a}{2}(\boldsymbol{\tau} - \boldsymbol{\beta}\Delta T) : \widehat{\boldsymbol{M}} : \dfrac{\partial \widehat{\boldsymbol{M}}^{-1}}{\partial \hat{\phi}} : \mathbb{C}^{-1} : (\boldsymbol{\tau} + \boldsymbol{\beta}\Delta T)$

6. Generalized Kuhn–Tucker conditions for rate-dependent problems

$$\dot{\lambda}^{\mathrm{vp}} \geq 0, \quad f \leq 0 \quad \Leftrightarrow \quad \dot{\lambda}^{\mathrm{vp}} f = 0, \quad \dot{\lambda}^{\mathrm{vd}} \geq 0, \quad g \leq 0 \quad \Leftrightarrow \quad \dot{\lambda}^{\mathrm{vd}} g = 0$$

(*Continued*)

known, which are the converged values of the previous step, and the

Table 1. Continued.

7. Temperature evolution (adiabatic condition)

$$\rho_0 c_p \dot{T} = \Upsilon \tau' : \left(\boldsymbol{d}^{vp} + \boldsymbol{d}^{vd}\right) - J^e P(\boldsymbol{d}^e : \mathbf{1}) - T\boldsymbol{\beta} : \boldsymbol{d}^e + \sum_{k=3}^{10} V_k \overset{\nabla}{\aleph}_k, \text{ where } V_k = T\frac{\partial \Sigma_k}{\partial T} - \Sigma_k$$

8. Equation of state (thermodynamic pressure)

$$P = (1-\gamma) c_v T^{ig} \varepsilon^e \text{ with } \varepsilon^e = 1/J^e - 1$$

$$T^{ig} = T_r \exp[(\eta - \eta_r)/c_v]\left[1 + \varepsilon^e\right]^{(\gamma-1)} \exp\left[(\gamma-1)(1/(1+\varepsilon^e) - 1)\right]$$

9. Failure criteria

$$\left\|\hat{\phi}\right\| = \sqrt{\hat{\phi}_{ij}\hat{\phi}_{ij}} \geq \left\|\phi\right\|_c \text{ and/or } P \geq P_{cutoff}$$

solution must be computed at t_{n+1} for a given body load increment, $\Delta \boldsymbol{b}$, and surface load increment, $\Delta \boldsymbol{t}$.

Let the dynamic evolution of a hypoelastic-thermo-viscoplastic and thermoviscodamaged body of volume V and surface S be governed at step time $n+1$, by the derived constitutive relations in Table 1 and by the following momentum, initial, and compatibility relations:

$$\boldsymbol{L}^T \boldsymbol{\tau}_{n+1} + \rho_0 \boldsymbol{b}_{n+1} = \rho_0 \dot{\boldsymbol{v}}_{n+1} \quad \text{in } V; \qquad \boldsymbol{t}_{n+1} = \boldsymbol{\tau}_{n+1}\boldsymbol{n} \quad \text{on } S_t \tag{1}$$

$$\boldsymbol{u} = \boldsymbol{u}_0, \qquad \boldsymbol{v} = \boldsymbol{v}_0 \quad \text{at } t = t_0 \tag{2}$$

$$\boldsymbol{l}_{n+1} = \nabla \boldsymbol{v}_{n+1} = \boldsymbol{C}\boldsymbol{v}_{n+1} \quad \text{in } V \tag{3}$$

$$\begin{aligned} &\boldsymbol{u}_{n+1} = \tilde{\boldsymbol{u}} \quad \text{on } S_u; \qquad \boldsymbol{v}_{n+1} = \tilde{\boldsymbol{v}} \quad \text{on } S_v; \\ &T_{n+1} = \tilde{T} \quad \text{on } S_T; \qquad \boldsymbol{q}_{n+1} = \tilde{\boldsymbol{q}} \quad \text{on } S_q \end{aligned} \tag{4}$$

where $(\cdot)_{n+1} = (\cdot)_n + \Delta(\cdot)$ is the additive decomposition of each of the internal variables. For algorithmic convenience, we have shifted to matrix vector notation in this section. Equations (1) express the discrete dynamic motion in the volume V and equilibrium on the free part of the boundary S_t at $n+1$. Viscohypoelasticity is not considered in this study; viscous damping effects are neglected. $\boldsymbol{L}$ is the differential operator, $\boldsymbol{b}$ and $\boldsymbol{t}$ are the body force and the surface traction vectors, respectively, $\boldsymbol{u}$ is the three-component displacement vector, and $\boldsymbol{n}$ denotes the outward normal to the surface S. The initial conditions on displacements and velocities are given by

Equations (2). The compatibility relation in volume V is given by Equation (3). The boundaries S_u, S_v, S_T, and S_q are parts of the boundary where the displacement $\tilde{\boldsymbol{u}}$, the velocity $\tilde{\boldsymbol{v}}$, the temperature $\tilde{T}$, and the heat flux $\tilde{\boldsymbol{q}}$ is prescribed, respectively. It is clear that $S_t \cup S_u \cup S_v \cup S_T \cup S_q = S$, $S_t \cap S_u = 0$, and $S_T \cap S_q = 0$.

In the context of the finite element method, the discrete problem can be obtained via a spatial Galerkin-type (displacement-based) projection of the semidiscrete (i.e., discrete in space and continuous in time) problem into a finite dimensional subspace of admissible continuous shape functions. Consequently, in the following sections the procedure for solving the derived set of governing equations using the finite element method are outlined. To integrate the set of constitutive equations in Table 1, a return mapping algorithm is developed in the subsequent section.

Numerical Integration of the Constitutive Model

Considering a given configuration of a known set of positions $\boldsymbol{X}$ at time t_n, the problem is now to update all state variables to a new configuration defined by its respective set of positions $\boldsymbol{x}$ (which are supposed to be known) at time t_{n+1}. This situation typically arises in a nonlinear finite element problem where the new positions $\boldsymbol{x}$ are determined from the discretized version of the momentum equation, Equation (1).

In this section, a new semi-implicit stress integration algorithm for rate-dependent problems is developed. This stress update algorithm treats the rate-independent and rate-dependent problems in a unified way. It is unified in the sense that the same routines are able to integrate both rate-independent and rate-dependent models by simply setting the viscosity parameters, η^{vp} and η^{vd}, to zero. Moreover, in this article we extend this algorithm to fully nonlocal coupled viscoplastic–viscodamage constitutive equations with a two-step predictor–corrector structure: hypoelastic predictor and coupled viscoplastic–viscodamage corrector (Zhu and Cescetto, 1995). In the model presented in this article, there exists two coupled surfaces, and for each iteration, the viscoplastic surface and the viscodamage surface should be corrected simultaneously (see Figure 1). The different steps of the integration algorithm are detailed here.

If the variables at iteration i, such as $\boldsymbol{\tau}_i$, $\widehat{\boldsymbol{X}}_i$, $\widehat{R}_i$, $\widehat{\boldsymbol{\phi}}_i$, $\widehat{\boldsymbol{H}}_i$, $\widehat{K}_i$, $\widehat{\boldsymbol{Y}}_i$, T_i, etc., are assumed to have been determined and the values of $\boldsymbol{d}$ and Δt are given, then $\boldsymbol{\tau}_{i+1}$ that satisfies the discretized constitutive equations can be obtained. In the following, a hypoelastic predictor and coupled viscoplastic–viscodamage corrector is proposed. In the first step, the hypoelastic predictor problem is solved with initial conditions that are the converged values of the previous iteration i while keeping irreversible variables frozen. This produces a trial

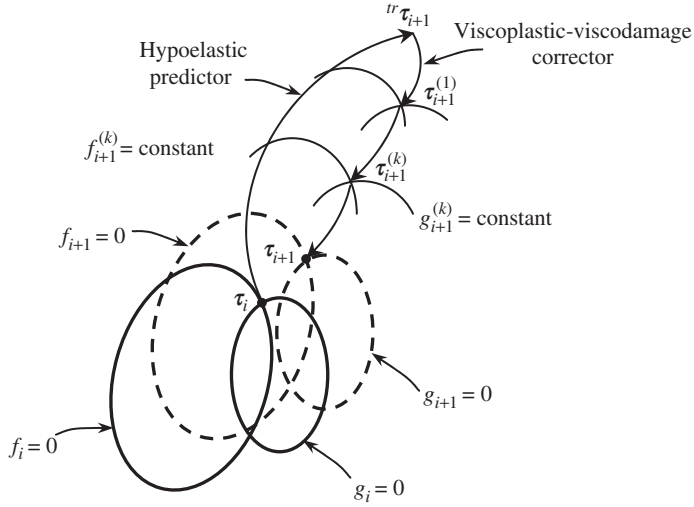

Figure 1. *Conceptual representation of the hypoelastic predictor and coupled viscoplastic–viscodamage corrector algorithm.*

stress state, $^{\mathrm{tr}}\boldsymbol{\tau}$, which, if outside the viscoplastic surface f and the viscodamage surface g is taken as the initial conditions for the solution of the viscoplastic–viscodamage corrector problem. The scope of this second step is to restore the generalized (i.e., rate-independent to rate-dependent problems) consistency condition by returning back the trial stress to the viscoplastic surface f and the viscodamage surface g simultaneously as conceptually represented in Figure 1.

However, one of the major challenges while integrating the constitutive equations in a finite deformation context is to achieve the incremental objectivity, i.e., to maintain correct rotational transformation properties all along a finite time step. A procedure that has now become very popular is first to rewrite the constitutive equations in a corotational moving frame. Given a skew-symmetric tensor $\boldsymbol{W} = -\boldsymbol{W}^T$ (e.g., $\boldsymbol{W} = \boldsymbol{\omega}$ where $\boldsymbol{\omega}$ is the spin tensor; $\boldsymbol{W} = \dot{\boldsymbol{R}}\boldsymbol{R}^T$; or the relative spin tensor $\boldsymbol{W} = \boldsymbol{\omega} - \dot{\boldsymbol{R}}\boldsymbol{R}^T$) such that it satisfies the relation $\mathbb{Q}\mathbb{Q}^T = \mathbb{Q}^T\mathbb{Q} = \boldsymbol{I}$, which if differentiated with respect to time yields

$$\boldsymbol{W} = \dot{\mathbb{Q}}\mathbb{Q}^T = -\mathbb{Q}\dot{\mathbb{Q}}^T = -\left(\dot{\mathbb{Q}}\mathbb{Q}^T\right)^T = -\boldsymbol{W}^T \tag{5}$$

Therefore, to ensure the orthogonality of the rotation matrix, we may generate a group of rotations $\mathbb{Q}$, by solving for

$$\dot{\mathbb{Q}} = \boldsymbol{W}\,\mathbb{Q} \quad \text{with} \quad \mathbb{Q}(t = t_n) = \mathbf{1} \tag{6}$$

It is now possible to generate a change of frame from the fixed Cartesian reference axes to the corresponding rotating axes (corotational axes). The Kirchhoff stress tensor $\boldsymbol{\tau}$ can then be transformed by $\mathbb{Q}$ as

$$\boldsymbol{\tau}^{\mathrm{c}} = \mathbb{Q}^T \boldsymbol{\tau}\, \mathbb{Q} \tag{7}$$

Differentiating the above equation with respect to time, we obtain

$$\dot{\boldsymbol{\tau}}^{\mathrm{c}} = \mathbb{Q}^T(\dot{\boldsymbol{\tau}} - \boldsymbol{W}\boldsymbol{\tau} + \boldsymbol{\tau}\boldsymbol{W})\mathbb{Q} = \mathbb{Q}^T \overset{\nabla}{\boldsymbol{\tau}}\, \mathbb{Q} \tag{8}$$

where $\overset{\nabla}{\boldsymbol{\tau}} = \dot{\boldsymbol{\tau}} - \boldsymbol{W}\boldsymbol{\tau} + \boldsymbol{\tau}\boldsymbol{W}$ is a corotational objective rate of the Kirchhoff stress.

In the literature many objective rates are introduced, such as Jaumann, Truesdell, and Green–Naghdi rates. From Equation (8) we can obtain the Jaumann rate if $\boldsymbol{W} = \boldsymbol{\omega}$ and the Green–Naghdi rate if $\boldsymbol{W} = \dot{\boldsymbol{R}}\boldsymbol{R}^T$. Moreover, Equation (8) indicates that a somewhat complicated expression as an objective derivative becomes a rather simple time derivative under the appropriate change of coordinates. This suggests that the entire theory and implementation will take on canonically simpler forms if transformed to the $\mathbb{Q}$-system. In the corotational frame, the rate of the corotational Kirchhoff stress is objective (frame-invariant), so that the stress rate equation takes the simpler form

$$\dot{\boldsymbol{\tau}}^{\mathrm{c}} = \mathbb{C}^{\mathrm{c}}\left(\boldsymbol{d}^{\mathrm{c}} - \boldsymbol{d}^{\mathrm{vp_c}} - \boldsymbol{d}^{\mathrm{vd_c}}\right) - \boldsymbol{A}^{\mathrm{c}}\dot{\boldsymbol{\phi}}^{\mathrm{c}} - \boldsymbol{\beta}^{\mathrm{c}}\dot{T} \tag{9}$$

The second-order tensors $\boldsymbol{d}$, $\overset{\nabla}{\boldsymbol{\phi}}$, and $\boldsymbol{\beta}$ can then be rewritten in the unrotated frame as:

$$\boldsymbol{d}^{\mathrm{c}} = \mathbb{Q}^T \boldsymbol{d}\, \mathbb{Q}; \quad \dot{\boldsymbol{\phi}}^{\mathrm{c}} = \mathbb{Q}^T \overset{\nabla}{\boldsymbol{\phi}}\, \mathbb{Q}; \quad \boldsymbol{\beta}^{\mathrm{c}} = \mathbb{Q}^T \boldsymbol{\beta}\, \mathbb{Q} \tag{10}$$

The fourth-order tensors $\mathbb{C}$ and $\boldsymbol{A}$ are also expressed in terms of the corotational components as:

$$\mathbb{C}^{\mathrm{c}} = \mathbb{Q}\left(\mathbb{Q}^T \mathbb{C}\mathbb{Q}\right)\mathbb{Q}^T = \mathbb{C}; \quad \boldsymbol{A}^{\mathrm{c}} = \mathbb{Q}\left(\mathbb{Q}^T \boldsymbol{A}\mathbb{Q}\right)\mathbb{Q}^T = \boldsymbol{A} \tag{11}$$

ELASTIC PREDICTOR

Assuming that the variables of the model at iteration i and the displacement field $\boldsymbol{u} = \boldsymbol{x}_{i+1} - \boldsymbol{x}_i$ at iteration $i+1$ are known, the trial elastic stress can then be given in the corotational frame by

$${}^{\mathrm{tr}}\boldsymbol{\tau}^{\mathrm{c}}_{i+1} = \boldsymbol{\tau}^{\mathrm{c}}_i + \mathbb{C}^{\mathrm{c}}_i : \boldsymbol{d}^{\mathrm{c}} \Delta t \tag{12}$$

or, in the Cartesian frame, the trial stress can be written as follows

$$ {}^{\mathrm{tr}}\tau_{i+1} = \mathbb{Q}_{i+1}\, {}^{\mathrm{tr}}\tau^{\mathrm{c}}_{i+1}\, \mathbb{Q}^{T}_{i+1} = \mathbb{Q}_{i+1}\big(\mathbb{Q}^{T}_{i}\tau_i\,\mathbb{Q}_i + \mathbb{C}^{\mathrm{c}}_i : \boldsymbol{d}^{\mathrm{c}}\Delta t\big)\mathbb{Q}^{T}_{i+1} \tag{13} $$

Using the polar decomposition $\boldsymbol{F} = \boldsymbol{R}\boldsymbol{U}$, we can write

$$ \boldsymbol{d}^{\mathrm{c}} = \mathbb{Q}^{T}\boldsymbol{d}\,\mathbb{Q} = \frac{1}{2}\mathbb{Q}^{T}\boldsymbol{R}\big(\dot{\boldsymbol{U}}\boldsymbol{U}^{-1} + \boldsymbol{U}^{-1}\dot{\boldsymbol{U}}\big)\boldsymbol{R}^{T}\mathbb{Q} \tag{14} $$

Equation (13) can then be simplified in the following way. Let us assume that the reference configuration is the configuration at i (update Lagrangian formulation), which implies that $\mathbb{Q}_i = \mathbf{1}$. Moreover, if we assume $\mathbb{Q}_{i+1} = \boldsymbol{R}$, this reduces Equation (14) to

$$ \boldsymbol{d}^{\mathrm{c}} = \frac{1}{2}\big(\dot{\boldsymbol{U}}\boldsymbol{U}^{-1} + \boldsymbol{U}^{-1}\dot{\boldsymbol{U}}\big) \tag{15} $$

A simple expression for the trial stress, Equation (13), can be obtained by adapting the following assumptions. Let us assume the following exponential map of the right stretch tensor, $\boldsymbol{U}(t)$, such that (Simo and Hughes, 1998):

$$ \boldsymbol{U}(t) = \exp\Big(\frac{t - t_n}{\Delta t}\boldsymbol{E}\Big) \tag{16} $$

where $\boldsymbol{E}$ is a constant tensor to be determined. Upon time differentiation of Equation (16), we obtain

$$ \dot{\boldsymbol{U}}(t) = \frac{\boldsymbol{E}}{\Delta t}\exp\Big(\frac{t - t_n}{\Delta t}\boldsymbol{E}\Big) \tag{17} $$

Substituting the above equation into Equation (15), yields

$$ \boldsymbol{d}^{\mathrm{c}} = \frac{\boldsymbol{E}}{\Delta t} \tag{18} $$

The tensor $\boldsymbol{E}$ is simply determined using the following compatibility conditions:

(a) in the reference configuration $(\boldsymbol{X}, t_n)$: $\boldsymbol{U}(t_n) = \exp(\mathbf{0}) = \mathbf{1}$
(b) in the current configuration $(\boldsymbol{x}, t_{n+1})$: $\boldsymbol{U}(t_{n+1}) = \exp(\boldsymbol{E})$

From these two conditions, we obtain

$$ \boldsymbol{E} = \ln \boldsymbol{U} = \frac{1}{2}\ln \boldsymbol{U}^2 = \frac{1}{2}\ln\big(\boldsymbol{F}^{T}\boldsymbol{F}\big) \tag{19} $$

which implies that $\boldsymbol{E}$ is the (incremental) natural strain tensor between the reference configuration and the current one. Hence, the trial elastic stress tensor in Equation (13) can be evaluated by:

$$^{\mathrm{tr}}\boldsymbol{\tau}_{i+1} = \boldsymbol{R}(\boldsymbol{\tau}_i + \mathbb{C}_i : \boldsymbol{E})\boldsymbol{R}^T \tag{20}$$

The final mapped stress is given in Equation (22).

In the above procedure, it is essential to realize that:

- $\boldsymbol{F} = \boldsymbol{R}\boldsymbol{U}$ are incremental tensors;
- it can be seen from Equation (19) that the proposed procedure is trivially incrementally objective. In the case of rigid body motion, $\boldsymbol{U}_{n+1} = \boldsymbol{U}_n$ and $\boldsymbol{d}^{\mathrm{c}} = \boldsymbol{0}$ or $\ln \boldsymbol{U} = \boldsymbol{0}$, thus the stress tensor will be updated exactly by the relation $\boldsymbol{\tau}_{n+1} = \boldsymbol{R}\,\boldsymbol{\tau}_n\boldsymbol{R}^T$, whatever the amplitude of the rotation;
- the rotation tensor $\boldsymbol{R}$ is directly and exactly computed from the polar decomposition and not from the (approximate) numerical integration of the rate equation $\dot{\mathbb{Q}} = \boldsymbol{W}\mathbb{Q}$ over the time interval $[t_n, t_{n+1}]$;
- in the proposed procedure, $\boldsymbol{R}$ only needs to be evaluated once per time step. This is different from the schemes proposed in Simo and Hughes (1998), where it needs to be evaluated twice per time step;
- all kinematic quantities are based on the deformation gradient $\boldsymbol{F}$ over the considered time step, a quantity that is readily available in a nonlinear finite element code, such as ABAQUS.

COUPLED VISCOPLASTIC–VISCODAMAGE CORRECTOR

Now if $f(^{\mathrm{tr}}\tau_{i+1}, \hat{\boldsymbol{X}}_i, \hat{R}_i, \hat{p}, T_i, \hat{\boldsymbol{\phi}}_i) \leq 0$ and $g(^{\mathrm{tr}}\hat{Y}_{i+1}, \hat{\boldsymbol{H}}_i, \hat{K}_i, \hat{r}_i, T_i, \hat{\boldsymbol{\phi}}_i) \leq 0$, the process is clearly undamaged elastic and the trial stress is in fact the final state. On the other hand, if $f > 0$ and $g > 0$, the Kuhn–Tucker loading/unloading conditions are violated by the trial stress, which now lies outside the generalized viscoplastic and viscodamge surfaces (Figure 1). Consistency, is restored by a generalization of the classical return mapping algorithm to rate-dependent problems. The coupled viscoplastic–viscodamge corrector problem may then be rephrased as (the objective rates reduce to a simple time derivative due to the fact that the global configuration is held fixed):

$$\begin{aligned}\dot{\boldsymbol{\tau}} &= -\mathbb{C} : \left(\boldsymbol{d}^{\mathrm{vp}} + \boldsymbol{d}^{\mathrm{vd}}\right) - \boldsymbol{A} : \dot{\boldsymbol{\phi}} - \boldsymbol{\beta}\dot{T} \\ &= -\mathbb{C} : \left(\dot{\lambda}^{\mathrm{vp}}\frac{\partial f}{\partial \boldsymbol{\tau}} + \dot{\lambda}^{\mathrm{vd}}\frac{\partial g}{\partial \boldsymbol{\tau}}\right) - \boldsymbol{A} : \left(\dot{\lambda}^{\mathrm{vp}}\frac{\partial f}{\partial \boldsymbol{Y}} + \dot{\lambda}^{\mathrm{vd}}\frac{\partial g}{\partial \boldsymbol{Y}}\right) - \boldsymbol{\beta}\dot{T}\end{aligned} \tag{21}$$

where $\dot{T}$ is calculated from the heat balance equation, while $\dot{\lambda}^{\mathrm{vp}}$ and $\dot{\lambda}^{\mathrm{vd}}$ are calculated, in a later section, using a nonlocal computational algorithm.

The hypoelastic predictor and coupled viscoplastic–viscodamage corrector step yields the final stress as:

$$\boldsymbol{\tau}_{i+1} = {}^{\mathrm{tr}}\boldsymbol{\tau}_{i+1} - \mathbb{C}_{i+1} : \left(\dot{\lambda}^{\mathrm{vp}} \frac{\partial f}{\partial \boldsymbol{\tau}} + \dot{\lambda}^{\mathrm{vd}} \frac{\partial g}{\partial \boldsymbol{\tau}} \right) - \boldsymbol{A}_{i+1} : \left(\dot{\lambda}^{\mathrm{vp}} \frac{\partial f}{\partial \boldsymbol{Y}} + \dot{\lambda}^{\mathrm{vd}} \frac{\partial g}{\partial \boldsymbol{Y}} \right) - \boldsymbol{\beta}_{i+1} \dot{T} \tag{22}$$

In the following sequence, we will show the procedure how to calculate the inelastic multipliers $\dot{\lambda}^{\mathrm{vp}}$ and $\dot{\lambda}^{\mathrm{vd}}$ using the adiabatic heating condition, the generalized viscoplastic consistency condition, and the generalized viscodamage consistency condition.

To establish the actual heat generation that occurs during the highly transient impact events of the thermomechanically coupled finite element, discretization of the heat equation is imperative. Since the whole impact process lasts a few hundreds of microseconds, the effect of heat conduction is negligible over the domain of the specimen. By only considering adiabatic heating with no external heat source along with $\boldsymbol{d}^{\mathrm{e}} = \boldsymbol{d} - \boldsymbol{d}^{\mathrm{vp}} - \boldsymbol{d}^{\mathrm{vd}}$, the heat balance equation can then be rewritten as:

$$\rho_{\mathrm{o}} c_{\mathrm{p}} \dot{T} = (\Upsilon \boldsymbol{\tau}' + J^{\mathrm{e}} P \mathbf{1} + T_i \boldsymbol{\beta}) : \left(\boldsymbol{d}^{\mathrm{vp}} + \boldsymbol{d}^{\mathrm{vd}} \right) - (J^{\mathrm{e}} P \mathbf{1} + T \boldsymbol{\beta}) : \boldsymbol{d} + \sum_{k=3}^{10} V_k \overset{\nabla}{\aleph}_k \tag{23}$$

where $V_k = T \partial \Sigma_k / \partial T - \Sigma_k \quad (k = 3, \ldots, 10)$ and their expressions are similar to those outlined in Table 4 of Part I, but instead of ϑ we substitute $\tilde{\vartheta} = T(\partial \vartheta / \partial T) - \vartheta$, and their magnitudes are obtained from the previous iteration i.

By making use of the evolution equations for $\boldsymbol{d}^{\mathrm{vp}}$, $\boldsymbol{d}^{\mathrm{vd}}$, and $\overset{\nabla}{\aleph}_k$ $(k = 3, \ldots, 10)$ given in Part I of the companion article, i.e., $\dot{p}$, $\nabla^2 \dot{p}$, $\overset{\nabla}{\boldsymbol{\alpha}}$, $\nabla^2 \overset{\nabla}{\boldsymbol{\alpha}}$, $\dot{r}$, $\nabla^2 \dot{r}$, $\overset{\nabla}{\boldsymbol{\Gamma}}$, and $\nabla^2 \overset{\nabla}{\boldsymbol{\Gamma}}$, the temperature evolution from Equation (23) can then be reduced to:

$$\dot{T} = -\frac{1}{\rho_{\mathrm{o}} c_{\mathrm{p}}} (J^{\mathrm{e}} P \mathbf{1} + T \boldsymbol{\beta}) : \boldsymbol{d} + Q_1^{\mathrm{tp}} \dot{\lambda}^{\mathrm{vp}} + Q_2^{\mathrm{tp}} \nabla^2 \dot{\lambda}^{\mathrm{vp}} + Q_1^{\mathrm{td}} \dot{\lambda}^{\mathrm{vd}} + Q_2^{\mathrm{td}} \nabla^2 \dot{\lambda}^{\mathrm{vd}} \tag{24}$$

where Q_k^{tp} and Q_k^{td} $(k = 1, 2)$ are obtained from the previous iteration i and are given by Equations (A-1)–(A-4) in the Appendix.

Moreover, we require the satisfaction of the generalized viscoplasticity consistency condition, $\dot{f}$, at the end of iteration $i+1$, such that

$$\frac{\partial f}{\partial \boldsymbol{\tau}} : \overset{\triangledown}{\boldsymbol{\tau}} + \left[\frac{\partial f}{\partial p} + \frac{1}{\Delta t}\frac{\partial f}{\partial \dot{p}}\right]\dot{p} + \left[\frac{\partial f}{\partial \nabla^2 p} + \frac{1}{\Delta t}\frac{\partial f}{\partial \nabla^2 \dot{p}}\right]\nabla^2 \dot{p} + \frac{\partial f}{\partial \boldsymbol{\alpha}} : \overset{\triangledown}{\boldsymbol{\alpha}} + \frac{\partial f}{\partial \nabla^2 \boldsymbol{\alpha}} : \overset{\triangledown}{\nabla^2 \boldsymbol{\alpha}}$$
$$+ \frac{\partial f}{\partial \boldsymbol{\phi}} : \overset{\triangledown}{\boldsymbol{\phi}} + \frac{\partial f}{\partial \nabla^2 \boldsymbol{\phi}} : \overset{\triangledown}{\nabla^2 \boldsymbol{\phi}} + \frac{\partial f}{\partial T}\dot{T} = 0 \tag{25}$$

Since we are applying the local iteration process within the time step $t+\Delta t$ (i.e., at step $n+1$) and the updated Lagrangian formulation is used, $\dot{p} = \ddot{p}\,\Delta t$ and $\nabla^2 \dot{p} = \Delta t \nabla^2 \ddot{p}$ are used in obtaining Equation (25). Substitution of the stress rate equation, $\overset{\triangledown}{\boldsymbol{\tau}}$, from Table 1 and the evolution equations for $\dot{p}$, $\nabla^2 \dot{p}$, $\overset{\triangledown}{\boldsymbol{\alpha}}$, $\overset{\triangledown}{\nabla^2 \boldsymbol{\alpha}}$, $\dot{r}$, $\nabla^2 \dot{r}$, $\overset{\triangledown}{\boldsymbol{\phi}}$, and $\overset{\triangledown}{\nabla^2 \boldsymbol{\phi}}$ from Part I of the companion article along with Equation (24) into Equation (25) yields the following expression:

$$\left(\frac{\partial f}{\partial \boldsymbol{\tau}} : \boldsymbol{C} + \boldsymbol{Z}^p\right) : \boldsymbol{d} + Q_1^p \dot{\lambda}^{\mathrm{vp}} + Q_2^p \nabla^2 \dot{\lambda}^{\mathrm{vp}} + Q_3^p \dot{\lambda}^{\mathrm{vd}} + Q_4^p \nabla^2 \dot{\lambda}^{\mathrm{vd}} = 0 \tag{26}$$

where $\boldsymbol{Z}^p$ and Q_k^p $(k = 1, \ldots, 4)$ are obtained from the previous i iteration and are given by Equations (A-5)–(A-9) in the Appendix.

Similarly, the generalized viscodamage consistency condition $\dot{g}$ needs to be satisfied. Since the viscodamage driving forces $\hat{Y}$ is a function of $\boldsymbol{\tau}$ and $\hat{\boldsymbol{\phi}}$, we can then express $\dot{g}$ around $(\hat{Y}, r, \nabla^2 r, \dot{r}, \nabla^2 \dot{r}, \boldsymbol{\Gamma}, \nabla^2 \boldsymbol{\Gamma}, \boldsymbol{\phi}, \nabla^2 \boldsymbol{\phi}, T)$ as follows:

$$\dot{g} \equiv \frac{\partial g}{\partial \boldsymbol{\tau}} : \overset{\triangledown}{\boldsymbol{\tau}} + \left(\frac{\partial g}{\partial r} + \frac{1}{\Delta t}\frac{\partial g}{\partial \dot{r}}\right)\dot{r} + \left(\frac{\partial g}{\partial \nabla^2 r} + \frac{1}{\Delta t}\frac{\partial g}{\partial \nabla^2 \dot{r}}\right)\nabla^2 \dot{r} + \frac{\partial g}{\partial \boldsymbol{\Gamma}} \overset{\triangledown}{\boldsymbol{\Gamma}} + \frac{\partial g}{\partial \nabla^2 \boldsymbol{\Gamma}} : \overset{\triangledown}{\nabla^2 \boldsymbol{\Gamma}}$$
$$+ \frac{\partial g}{\partial \boldsymbol{\phi}} : \overset{\triangledown}{\boldsymbol{\phi}} + \frac{\partial g}{\partial \nabla^2 \boldsymbol{\phi}} : \overset{\triangledown}{\nabla^2 \boldsymbol{\phi}} + \frac{\partial g}{\partial T}\dot{T} = 0 \tag{27}$$

Substitution of the stress rate equation, $\overset{\triangledown}{\boldsymbol{\tau}}$, from Table 1 and the evolution equations for $\dot{r}$, $\nabla^2 \dot{r}$, $\overset{\triangledown}{\boldsymbol{\Gamma}}$, $\overset{\triangledown}{\nabla^2 \boldsymbol{\Gamma}}$, $\overset{\triangledown}{\boldsymbol{\phi}}$, and $\overset{\triangledown}{\nabla^2 \boldsymbol{\phi}}$ from Part I of the companion article along with Equation (24) into Equation (27) yields the following expression:

$$\left(\frac{\partial g}{\partial \boldsymbol{\tau}} : \boldsymbol{C} + \boldsymbol{Z}^d\right) : \boldsymbol{d} + Q_1^d \dot{\lambda}^{\mathrm{vp}} + Q_2^d \nabla^2 \dot{\lambda}^{\mathrm{vp}} + Q_3^d \dot{\lambda}^{\mathrm{vd}} + Q_4^d \nabla^2 \dot{\lambda}^{\mathrm{vd}} = 0 \tag{28}$$

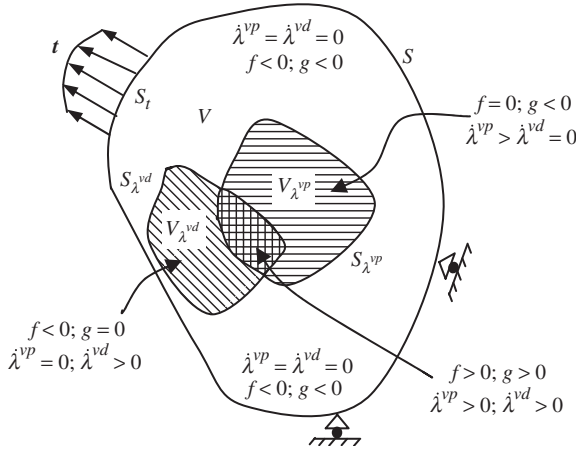

Figure 2. *Schematic representation of elastic, viscoplastic, and viscodamage boundaries.*

where $\boldsymbol{Z}^d$ and Q_k^d $(k = 1, \ldots, 4)$ are obtained from the previous i iteration and are given by Equations (A-10)–(A-14) in the Appendix.

Owing to the higher order of the governing equations, Equations (24), (26), and (28), in the inelastic region, considerable difficulties are experienced with their numerical implementation. The consistency condition of inelasticity is no longer an algebraic equation but is a differential one because of $\nabla^2\dot{\lambda}^{\mathrm{vp}}$ and $\nabla^2\dot{\lambda}^{\mathrm{vd}}$, which needs to be calculated along with $\dot{\lambda}^{\mathrm{vp}}$ and $\dot{\lambda}^{\mathrm{vd}}$. Another complication is the higher-order boundary conditions that are necessary from the mathematical point of view and have to be prescribed on the moving elasto-inelastic boundary (Figure 2). These internal boundaries are not always easy to interpret physically. The computational technique usually followed for integrating the gradient-enhanced constitutive relations was first proposed by de Borst and coworkers (e.g., de Borst and Mühlhaus, 1992; de Borst et al., 1993, 1999; Pamin 1994; de Borst and Pamin, 1996; Peerlings et al., 1996; Pamin et al., 2003; and the references quoted therein). In their works, the plasticity yield and/or damage growth conditions depend on the Laplacian of an equivalent kinematic measure (hardening/softening state variables), and the consistency conditions result in differential equations with respect to the plastic/damage multipliers. The multipliers, $\dot{\lambda}^{\mathrm{vp}}$ and/or $\dot{\lambda}^{\mathrm{vd}}$, are considered as fundamental unknowns (additional degrees of freedom) having a role similar to that of displacements and are discretized in addition to the usual discretization of the displacements. In addition, the consistency condition is written in a weak form and solved simultaneously with the equation of motion. However, because of the presence of high-order derivatives in the weak form of the (initial) boundary value problem,

there is a need for numerically expensive C^1-continuous conditions on the shape functions or penalty-enhanced C^0 class functions for the interpolation of the plastic/damage multipliers (or other field variables, such as stress and strain) in the finite element context. Moreover, C^2 and higher continuity are also needed if fourth-order or higher-order gradient terms are incorporated, otherwise the gradient terms lose their presence. Therefore, in the de Borst approach Hermitian or mixed formulations are unavoidable for a consistent finite element formulation and, for the inelastic process, a standard return mapping algorithm is performed, in which the values of the kinematic fields at an integration point are interpolated from their nodal values. This approach has been discussed thoroughly by Voyiadjis et al. (2001, 2003, 2004) and used intensively by many other authors (e.g., Comi and Perego, 1996; Mikkelsen, 1997; Ramaswamy and Aravas, 1998a,b; Svedberg and Runesson, 2000; Nedjar, 2001; Zervos et al., 2001; Chen and Yuan, 2002; Matsushima et al., 2002; Liebe et al., 2003; and the references quoted therein). The disadvantage of this approach is that it gives rise to many numerical difficulties that require considerable modifications to the existing finite element codes, which make their implementation not an easy or direct task.

We are looking for an alternative, simple, and robust numerical algorithm for the computation of the higher-order gradient terms, $\nabla^2\dot{\lambda}^{vp}$ and $\nabla^2\dot{\lambda}^{vd}$, without the need for large modifications of the finite element procedure, which makes the gradient approach comparatively easy and attractive to implement in an existing finite element program, such as ABAQUS. The main purpose of the next section is, therefore, to describe a new algorithmic implementation of the gradient-based models.

COMPUTATION OF THE LAPLACIAN OF VISCOPLASTICITY AND VISCODAMAGE MULTIPLIERS

In this section, we will show how we can compute the Laplacian terms $\nabla^2\dot{\lambda}^{vp}$ and $\nabla^2\dot{\lambda}^{vd}$ using a simple and robust approach that is proposed by Abu Al-Rub and Voyiadjis (2005).

In the approach followed in this article, the nonlocal consistency condition is transformed into a linear set of equations that depends on the material parameters and on the current coordinates of the integration points. These sets of linear equations are solved by any numerical iterative method for the inelastic multipliers of the integration points that exist in a global (nonlocal) superelement of eight adjacent local elements in a nonlocal sense (Figure 3). The gradient terms, $\nabla^2\dot{\lambda}^{vp}$ and $\nabla^2\dot{\lambda}^{vd}$, at each integration point in the local element are evaluated from the derivatives of a polynomial that interpolates the value of the inelastic multiplier, $\dot{\lambda}^{vp}$ and $\dot{\lambda}^{vd}$, in the superelement with classical integration points. In addition, this procedure

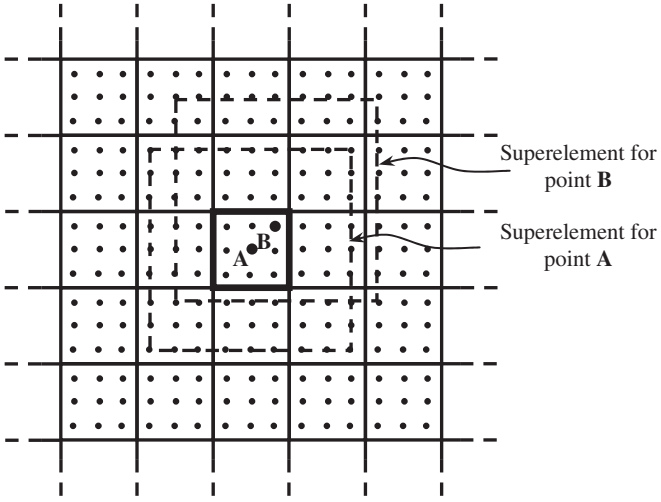

Figure 3. *A schematic illustration for the computation of the Laplacian terms from a regular finite element mesh.*

enforces the generalized consistency conditions, $\dot{f}$ and $\dot{g}$, in the sense of distributions, i.e., f and g are satisfied at the end of the loading step. However, in this approach there in no need to consider the inelastic multipliers as additional degrees of freedom. Therefore, by using this approach, we do not need to introduce high-order continuous shape functions (e.g., C^1 class or penalty-enhanced C^0 class functions) for the interpolation of the multiplier fields in the finite element context. In consequence, a straightforward one-field C^0-continuous finite element implementation can be easily used. Furthermore, this algorithm has the major advantage that it avoids boundary conditions on the moving elasto-inelastic boundary since the resulting partial differential equations hold in the whole body.

The inelastic multipliers are not considered here as independent global variables but as local internal variables. In classical inelasticity, the inelastic multipliers are calculated by restoring the consistency condition iteratively. However, for the nonlocal formulation, it is not possible because it depends on high-order gradients. To evaluate the gradients $\nabla^2\dot{\lambda}^{\mathrm{vp}}$ and $\nabla^2\dot{\lambda}^{\mathrm{vd}}$ at integration point m, we need the values of $\dot{\lambda}^{\mathrm{vp}}$ and $\dot{\lambda}^{\mathrm{vd}}$ at point m as well as the values at the neighboring points (nonlocality). The gradient at each integration point m is evaluated from the derivatives of a polynomial function that interpolates the values of the inelastic multiplier at the neighboring points. Therefore, the gradient terms, $\nabla^2\dot{\lambda}^{\mathrm{vp}}$ and $\nabla^2\dot{\lambda}^{\mathrm{vd}}$, can be

expressed in terms of $\dot{\lambda}_n^{\mathrm{vp}}$ and $\dot{\lambda}_n^{\mathrm{vd}}$ with $n \in \{1, \ldots, N_{\mathrm{GP}}\}$ using the following relations:

$$\nabla^2 \dot{\lambda}_m^{\mathrm{vp}} = \sum_{n=1}^{N_{\mathrm{GP}}} \bar{g}_{mn} \dot{\lambda}_n^{\mathrm{vp}}; \qquad \nabla^2 \dot{\lambda}_m^{\mathrm{vd}} = \sum_{n=1}^{N_{\mathrm{GP}}} \bar{g}_{mn} \dot{\lambda}_n^{\mathrm{vd}} \tag{29}$$

where N_{GP} is the number of Gauss integration points. The computation of coefficients $\bar{g}_{mn}$ is explained in what follows.

Figure 3 shows a schematic illustration for the computation of the Laplacian terms from a regular finite element mesh, where $\nabla^2 \dot{\lambda}^{\mathrm{vp}}$ and $\nabla^2 \dot{\lambda}^{\mathrm{vd}}$ are needed at the integration points of each element. For two-dimensional problems four-noded element with nine integration points (full integration) is assumed. Eight elements (superelement) are used to compute $\nabla^2 \dot{\lambda}^{\mathrm{vp}}$ and $\nabla^2 \dot{\lambda}^{\mathrm{vd}}$ at each integration point. This means that 81 integration points are used to calculate the gradients at each integration point. Except for each corner and mid-boundary elements, their nine integration points are used to calculate the gradients. This illustration is valid for any element with any number of integration points. However, with more integration points, higher accuracy is achieved. This illustration is valid for one-dimensional as well as for three-dimensional mesh discretizations. However, the disadvantage of this approach is that regular meshes are required and with large precision loss for complicated problems, which limits the applicability of this approach. More elaborate studies are needed to generalize this approach to non-regular mesh discretizations. This is not the subject of this study but it will be presented in a forthcoming article by the authors.

To determine the coefficients $\bar{g}_{mn}$, a complete second-order polynomial function is used to evaluate the inelastic multipliers around point m, such that

$$\dot{\lambda} = \boldsymbol{a}^T \boldsymbol{v} \tag{30}$$

where $\dot{\lambda}$ could be $\dot{\lambda}^{\mathrm{vp}}$ or $\dot{\lambda}^{\mathrm{vd}}$, $\boldsymbol{a}$ is the coefficients vector, and $\boldsymbol{v}$ is the variables vector. For example in two-dimensional problems, we have the following expressions for $\boldsymbol{a}$ and $\boldsymbol{v}$: $\boldsymbol{a}^T = \lfloor a_1 \ a_2 \ a_3 \ a_4 \ a_5 \ a_6 \rfloor$ and $\boldsymbol{v}^T = \lfloor 1 \ x \ y \ xy \ x^2 \ y^2 \rfloor$.

To obtain the coefficients vector $\boldsymbol{a}$, a minimization method by least squares is used. Moreover, the interpolation is made in the global coordinate system (x, y, z) of the generated mesh with N_{GP} integration points. The coefficients vector $\boldsymbol{a}$ can be expressed in the following form:

$$\boldsymbol{\Lambda} = \boldsymbol{M}^T \boldsymbol{a} \tag{31}$$

For a two-dimensional mesh, the matrix $\boldsymbol{M}$ and the inelastic multipliers vector $\boldsymbol{\Lambda}$ are defined by

$$\boldsymbol{M} = \begin{bmatrix} 1 & 1 & \cdots & 1 \\ x_1 & x_2 & \cdots & x_{N_{\mathrm{GP}}} \\ y_1 & y_2 & \cdots & y_{N_{\mathrm{GP}}} \\ x_1 y_1 & x_2 y_2 & \cdots & x_{N_{\mathrm{GP}}} y_{N_{\mathrm{GP}}} \\ x_1^2 & x_2^2 & \cdots & x_{N_{\mathrm{GP}}}^2 \\ y_1^2 & y_2^2 & \cdots & y_{N_{\mathrm{GP}}}^2 \end{bmatrix} \tag{32}$$

and $\boldsymbol{\Lambda} = \begin{bmatrix} \dot{\lambda}_1 & \dot{\lambda}_2 & \cdots & \dot{\lambda}_{N_{\mathrm{GP}}} \end{bmatrix}^T$.

Multiplying both sides of Equation (31) by $\boldsymbol{M}$, we can write

$$\boldsymbol{M}\boldsymbol{\Lambda} = \boldsymbol{H}\boldsymbol{a} \tag{33}$$

with $\boldsymbol{H} = \boldsymbol{M}\boldsymbol{M}^T$ is a symmetrical square matrix and can be written for two-dimensional problems as:

$$\boldsymbol{H} = \sum_{n=1}^{N_{\mathrm{GP}}} \begin{bmatrix} 1 & x_n & y_n & x_n y_n & x_n^2 & y_n^2 \\ & x_n^2 & x_n y_n & x_n^2 y_n & x_n^3 & x_n y_n^2 \\ & & y_n^2 & x_n y_n^2 & x_n^2 y_n & y_n^3 \\ & & & x_n^2 y_n^2 & x_n^3 y_n & x_n y_n^3 \\ & \text{Symm} & & & x_n^4 & x_n^2 y_n^2 \\ & & & & & y_n^4 \end{bmatrix} \tag{34}$$

It is obvious that $\boldsymbol{H}$ needs to be updated at each loading increment for finite deformation problems.

From Equations (30) and (33), we can then compute the inelastic multiplier vector and its Laplacian, respectively, as follows:

$$\dot{\lambda} = \boldsymbol{a}^T \boldsymbol{v} = \left(\boldsymbol{H}^{-1}\boldsymbol{M}\boldsymbol{\Lambda}\right)^T \boldsymbol{v} = \left(\boldsymbol{H}^{-1} \sum_{n=1}^{N_{\mathrm{GP}}} \dot{\lambda}_n \boldsymbol{v}_n\right)^T \boldsymbol{v} \tag{35}$$

$$\nabla^2 \dot{\lambda} = \left(\boldsymbol{H}^{-1} \sum_{n=1}^{N_{\mathrm{GP}}} \dot{\lambda}_n \boldsymbol{v}_n\right)^T \nabla \boldsymbol{v} \tag{36}$$

For the integration point m, we can write expressions for

$$\nabla^2 \dot{\lambda}_m = \nabla_{xx} \dot{\lambda}_m + \nabla_{yy} \dot{\lambda}_m + \nabla_{zz} \dot{\lambda}_m \tag{37}$$

as follows

$$\nabla^2 \dot{\lambda}_m = \sum_{n=1}^{N_{GP}} \left(\boldsymbol{v}_n^T \boldsymbol{H}^{-1} \nabla_{xx} \boldsymbol{v}_m + \boldsymbol{v}_n^T \boldsymbol{H}^{-1} \nabla_{yy} \boldsymbol{v}_m + \boldsymbol{v}_n^T \boldsymbol{H}^{-1} \nabla_{zz} \boldsymbol{v}_m \right) \dot{\lambda}_n \tag{38}$$

Comparing Equations (29) with Equation (38), we can then compute the coefficients $\bar{g}_{mn}$ using the following expression:

$$\bar{g}_{mn} = \boldsymbol{v}_n^T \boldsymbol{H}^{-1} \nabla_{xx} \boldsymbol{v}_m + \boldsymbol{v}_n^T \boldsymbol{H}^{-1} \nabla_{yy} \boldsymbol{v}_m + \boldsymbol{v}_n^T \boldsymbol{H}^{-1} \nabla_{zz} \boldsymbol{v}_m \tag{39}$$

The coefficients $\bar{g}_{mn}$ depend only on the x, y, z updated coordinates of the Gauss integration points. These coefficients are computed at each loading increment for finite deformations.

Using Equations (29) and (39) we can now determine nonlocally $\dot{\lambda}^{vp}$ and $\dot{\lambda}^{vd}$ at each integration point m from the generalized consistency conditions, Equations (26) and (28). This is shown in the subsequent development.

NONLOCAL COMPUTATIONAL ALGORITHM

By substituting Equations (29) into Equations (26) and (28), we can then rewrite the generalized viscoplasticity consistency condition, Equation (26), and the generalized viscodamage consistency condition, Equation (28), at each integration point m, respectively, as follows:

$$\left(\frac{\partial f}{\partial \boldsymbol{\tau}_{(m)}^{(i)}} : \boldsymbol{C}_{(m)}^{(i)} + \boldsymbol{Z}_{(m)}^{p(i)} \right) : \boldsymbol{d}_{(m)} + Q_{1(m)}^{p(i)} \dot{\lambda}_{(m)}^{vp} + Q_{2(m)}^{p(i)} \sum_{n=1}^{N_{GP}} \bar{g}_{(mn)} \dot{\lambda}_{(n)}^{vp} + Q_{3(m)}^{p(i)} \dot{\lambda}_{(m)}^{vd} + Q_{4(m)}^{p(i)} \sum_{n=1}^{N_{GP}} \bar{g}_{(mn)} \dot{\lambda}_{(n)}^{vd} = 0 \tag{40}$$

$$\left(\frac{\partial g}{\partial \boldsymbol{\tau}_{(m)}^{(i)}} : \boldsymbol{C}_{(m)}^{(i)} + \boldsymbol{Z}_{(m)}^{d(i)} \right) : \boldsymbol{d}_{(m)} + Q_{1(m)}^{d(i)} \dot{\lambda}_{(m)}^{vp} + Q_{2(m)}^{d(i)} \sum_{n=1}^{N_{GP}} \bar{g}_{(mn)} \dot{\lambda}_{(n)}^{vp} + Q_{3(m)}^{d(i)} \dot{\lambda}^{vd} + Q_{4(m)}^{d(i)} \sum_{n=1}^{N_{GP}} \bar{g}_{(mn)} \dot{\lambda}_{(n)}^{vd} = 0 \tag{41}$$

Note that (m) indicates the integration point and (i) indicates the previous iteration number.

Let us define the following expressions:

$$\mathbb{R}^{p(i)}_{(m)} = \left(\frac{\partial f}{\partial \boldsymbol{\tau}^{(i)}_{(m)}} : \boldsymbol{C}^{(i)}_{(m)} + \boldsymbol{Z}^{p(i)}_{(m)} \right) : \boldsymbol{d}_{(m)} \tag{42}$$

$$\mathbb{R}^{d(i)}_{(m)} = \left(\frac{\partial g}{\partial \boldsymbol{\tau}^{(i)}_{(m)}} : \boldsymbol{C}^{(i)}_{(m)} + \boldsymbol{Z}^{d(i)}_{(m)} \right) : \boldsymbol{d}_{(m)} \tag{43}$$

$$\boldsymbol{G}^{pp(i)} = \begin{bmatrix} Q^{p(i)}_{1(1)} + Q^{p(i)}_{2(1)} \bar{g}_{11} & Q^{p(i)}_{2(2)} \bar{g}_{12} & \cdots & Q^{p(i)}_{2(N_{\mathrm{GP}})} \bar{g}_{1N_{\mathrm{GP}}} \\ Q^{p(i)}_{2(2)} \bar{g}_{21} & Q^{p(i)}_{1(2)} + Q^{p(i)}_{2(2)} \bar{g}_{22} & \cdots & Q^{p(i)}_{2(N_{\mathrm{GP}})} \bar{g}_{2N_{\mathrm{GP}}} \\ \vdots & \vdots & \ddots & \vdots \\ Q^{p(i)}_{2(N_{\mathrm{GP}})} \bar{g}_{N_{\mathrm{GP}}1} & Q^{p(i)}_{2(N_{\mathrm{GP}})} \bar{g}_{2N_{\mathrm{GP}}} & \cdots & Q^{p(i)}_{1(N_{\mathrm{GP}})} + Q^{p(i)}_{2(N_{\mathrm{GP}})} \bar{g}_{N_{\mathrm{GP}}N_{\mathrm{GP}}} \end{bmatrix} \tag{44}$$

$$\boldsymbol{G}^{pd(i)} = \begin{bmatrix} Q^{p(i)}_{3(1)} + Q^{p(i)}_{4(1)} \bar{g}_{11} & Q^{p(i)}_{4(2)} \bar{g}_{12} & \cdots & Q^{p(i)}_{4(N_{\mathrm{GP}})} \bar{g}_{1N_{\mathrm{GP}}} \\ Q^{p(i)}_{4(2)} \bar{g}_{21} & Q^{p(i)}_{3(2)} + Q^{p(i)}_{4(2)} \bar{g}_{22} & \cdots & Q^{p(i)}_{4(N_{\mathrm{GP}})} \bar{g}_{2N_{\mathrm{GP}}} \\ \vdots & \vdots & \ddots & \vdots \\ Q^{p(i)}_{4(N_{\mathrm{GP}})} \bar{g}_{N_{\mathrm{GP}}1} & Q^{p(i)}_{4(N_{\mathrm{GP}})} \bar{g}_{2N_{\mathrm{GP}}} & \cdots & Q^{p(i)}_{3(N_{\mathrm{GP}})} + Q^{p(i)}_{4(N_{\mathrm{GP}})} \bar{g}_{N_{\mathrm{GP}}N_{\mathrm{GP}}} \end{bmatrix} \tag{45}$$

$$\boldsymbol{G}^{dp(i)} = \begin{bmatrix} Q^{d(i)}_{1(1)} + Q^{d(i)}_{2(1)} \bar{g}_{11} & Q^{d(i)}_{2(2)} \bar{g}_{12} & \cdots & Q^{d(i)}_{2(N_{\mathrm{GP}})} \bar{g}_{1N_{\mathrm{GP}}} \\ Q^{d(i)}_{2(2)} \bar{g}_{21} & Q^{d(i)}_{1(2)} + Q^{d(i)}_{2(2)} \bar{g}_{22} & \cdots & Q^{d(i)}_{2(N_{\mathrm{GP}})} \bar{g}_{2N_{\mathrm{GP}}} \\ \vdots & \vdots & \ddots & \vdots \\ Q^{d(i)}_{2(N_{\mathrm{GP}})} \bar{g}_{N_{\mathrm{GP}}1} & Q^{d(i)}_{2(N_{\mathrm{GP}})} \bar{g}_{2N_{\mathrm{GP}}} & \cdots & Q^{d(i)}_{1(N_{\mathrm{GP}})} + Q^{d(i)}_{2(N_{\mathrm{GP}})} \bar{g}_{N_{\mathrm{GP}}N_{\mathrm{GP}}} \end{bmatrix} \tag{46}$$

$$\boldsymbol{G}^{dd(i)} = \begin{bmatrix} Q^{d(i)}_{3(1)} + Q^{d(i)}_{4(1)} \bar{g}_{11} & Q^{d(i)}_{4(2)} \bar{g}_{12} & \cdots & Q^{d(i)}_{4(N_{\mathrm{GP}})} \bar{g}_{1N_{\mathrm{GP}}} \\ Q^{d(i)}_{4(2)} \bar{g}_{21} & Q^{d(i)}_{3(2)} + Q^{d(i)}_{4(2)} \bar{g}_{22} & \cdots & Q^{d(i)}_{4(N_{\mathrm{GP}})} \bar{g}_{2N_{\mathrm{GP}}} \\ \vdots & \vdots & \ddots & \vdots \\ Q^{d(i)}_{4(N_{\mathrm{GP}})} \bar{g}_{N_{\mathrm{GP}}1} & Q^{d(i)}_{4(N_{\mathrm{GP}})} \bar{g}_{2N_{\mathrm{GP}}} & \cdots & Q^{d(i)}_{3(N_{\mathrm{GP}})} + Q^{d(i)}_{4(N_{\mathrm{GP}})} \bar{g}_{N_{\mathrm{GP}}N_{\mathrm{GP}}} \end{bmatrix} \tag{47}$$

$$\boldsymbol{\Lambda}^{\mathrm{vp}} = \left\lfloor \dot{\lambda}_1^{\mathrm{vp}} \quad \dot{\lambda}_2^{\mathrm{vp}} \quad \cdots \quad \dot{\lambda}_{N_{\mathrm{GP}}}^{\mathrm{vp}} \right\rfloor^T \tag{48}$$

$$\boldsymbol{\Lambda}^{\mathrm{vd}} = \left\lfloor \dot{\lambda}_1^{\mathrm{vd}} \quad \dot{\lambda}_2^{\mathrm{vd}} \quad \cdots \quad \dot{\lambda}_{N_{\mathrm{GP}}}^{\mathrm{vd}} \right\rfloor^T \tag{49}$$

$$\mathbb{R}^{p(i)} = \left\lfloor \mathbb{R}_1^{p(i)} \quad \mathbb{R}_2^{p(i)} \quad \cdots \quad \mathbb{R}_{N_{\mathrm{GP}}}^{p(i)} \right\rfloor^T \tag{50}$$

$$\mathbb{R}^{d(i)} = \left\lfloor \mathbb{R}_1^{d(i)} \quad \mathbb{R}_2^{d(i)} \quad \cdots \quad \mathbb{R}_{N_{\mathrm{GP}}}^{d(i)} \right\rfloor^T \tag{51}$$

We can then write Equations (40) and (41), respectively, as follows:

$$\boldsymbol{G}^{pp(i)}\boldsymbol{\Lambda}^{\mathrm{vp}} + \boldsymbol{G}^{pd(i)}\boldsymbol{\Lambda}^{\mathrm{vd}} = \mathbb{R}^{p(i)} \tag{52}$$

$$\boldsymbol{G}^{dp(i)}\boldsymbol{\Lambda}^{\mathrm{vp}} + \boldsymbol{G}^{dd(i)}\boldsymbol{\Lambda}^{\mathrm{vd}} = \mathbb{R}^{d(i)} \tag{53}$$

Combining Equations (52) and (53), we obtain

$$\begin{bmatrix} \boldsymbol{G}^{pp(i)} & \boldsymbol{G}^{pd(i)} \\ \boldsymbol{G}^{dp(i)} & \boldsymbol{G}^{dd(i)} \end{bmatrix} \begin{Bmatrix} \boldsymbol{\Lambda}^{\mathrm{vp}} \\ \boldsymbol{\Lambda}^{\mathrm{vd}} \end{Bmatrix} = \begin{Bmatrix} \mathbb{R}^{p(i)} \\ \mathbb{R}^{d(i)} \end{Bmatrix} \tag{54}$$

The above linear system of equations can be solved for $\boldsymbol{\Lambda}^{\mathrm{vp}}$ and $\boldsymbol{\Lambda}^{\mathrm{vd}}$ using a numerical iterative scheme such as the Gauss–Jordan iterative method. The viscoplastic and viscodamage multipliers are obtained when the viscoplasticity and viscodamage conditions, f and g, are fulfilled at the end of the loading step for a suitable tolerance, such that:

$$\sum_{n=1}^{N_{\mathrm{GP}}} f_n \leq \mathrm{TOL} \quad \text{and} \quad \sum_{n=1}^{N_{\mathrm{GP}}} g_n \leq \mathrm{TOL} \tag{55}$$

where TOL could be set to a very small value in the order of 10^{-5}.

Note that in the undamaged-elastic elements $\dot{\lambda}_m = 0$; however, for spreading of the inelastic zone it is important that the numerical solution allows $\nabla^2\dot{\lambda}_m > 0$ at the elastic–inelastic boundary. If inelastic integration points appear in the structure, then in the elastic integration points adjacent to the inelastic zone we have non-zero $\boldsymbol{\Lambda}$ (Figure 2). Therefore, the proposed algorithm has the feature, that these elastic integration points have $\dot{\lambda}_m \approx 0$ and $\nabla^2\dot{\lambda}_m > 0$. As a result, the yield strength is increased/decreased and the damage at these elastic points is delayed (hardening) or enters the softening region.

The above algorithm for gradient-dependent inelasticity appears to have several advantages over the standard algorithm by de Borst and his coworkers with regard to the incorporation of the gradient-dependent model in a finite element code. The proposed computational algorithm can

be implemented in the existing finite element codes without large modifications as compared to the computational approach of de Borst and his coworkers. In contrast to the later approach, for calculation of the gradient terms we do not need to introduce shape functions of the C^1 class or penalty-enhanced C^0 class functions for the interpolation of the gradient terms. This is because the governing constitutive equations in the proposed approach are replaced directly by the difference equations of the field variables and no interpolation functions are needed for the gradient terms.

NUMERICAL APPLICATIONS

In this section, some numerical examples are presented to verify the implementation of the proposed constitutive model using the commercial finite element program ABAQUS (2003). The algorithmic model presented in the previous section is coded as a VUMAT user material subroutine of ABAQUS/Explicit. The ABAQUS/Explicit is mainly used for high transient dynamic problems and it uses explicit integration algorithms. For information about writing the VUMAT subroutine, consult the reference manuals of ABAQUS/Explicit (2003).

The first two examples are related to the nonlocal hypoelasto-thermoviscoplastic (without damage) to show the efficiency of the model in obtaining mesh objective simulations. The first example demonstrates the use of the viscosity as a localization limiter, while the second example demonstrates the use of the gradient approach as a localization limiter. The third example is related to the whole model used to solve perforation of a steel target by a blunt projectile for different impact speeds.

Strip with a Fixed Edge

The role of the viscosity localization limiter in setting the character of the governing differential equations and in introducing a length-scale is illustrated by considering shear band development in a simple plane strain strip subjected to low impact loading. Of particular interest are ill-posed initial boundary value problems in hypoelastic and thermoviscoplastic solids (without damage).

Now let us consider a two-dimensional initial boundary value problem for a specimen of 100 mm length and 20 mm width (Figure 4(a)). The bottom side of the specimen is fixed and the topside is movable. The loading is enforced by a velocity profile shown in Figure 4(a) that acts at the free end of the specimen. Three mesh discretizations of 15×50, 25×70, and 30×100 meshes are used with eight-noded rectangular elements. The constitutive parameters used in the computation are listed in Table 2 for the

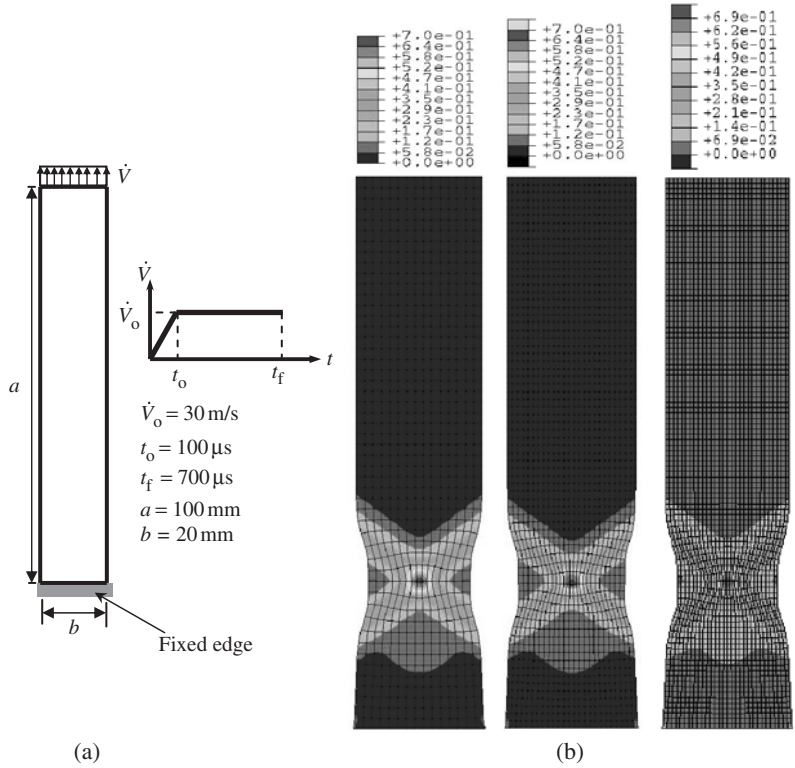

Figure 4. *Study of mesh sensitivity: (a) problem description of a strip with a fixed edge under impact tensile loading and (b) deformation patterns and contour plots of the effective viscoplastic strain for 15 × 50, 25 × 70, 30 × 100 finite element discretizations.*

target material (Weldox 460 E steel). Time increments of the order 10^{-8} s are used to satisfy the stability criteria. The results presented below are focused on the distribution of the effective viscoplastic strain at the final state of localization. Figure 4(b) shows clearly the localized regions of intense shear at the end of localization ($t_f = 700\,\mu$s). We can easily observe the intense equivalent viscoplastic strain distributions that show the width and the location of the shear band development. Note that due to the inhomogeneity introduced by the clamped boundary conditions, no geometric imperfections are needed to initiate localized deformation modes. For other cases, not reported here, for large viscosity the viscoplastic deformations are diffused over the whole specimen and the localization does not manifest itself.

The deformed configurations shown in Figure 4(b) indicate the formation of a neck and a pronounced shear band of almost a mesh independent band

Table 2. Material constants for target and projectile materials.

Target material of Weldox 460 E steel			
$E = 200$ GPa	$a_1 = 400$ MPa	$a = 98\ \mu m^2$	$h_1 = 0$
$\nu = 0.33$	$b_1 = 0.005$ N	$\Upsilon = 0.9$	$h_2 = 0$
$\bar{Y}_o = 490$ MPa	$k_1 = 0.1\ MPa^{-1}$	$\ell_1 = 5\ \mu m$	$\eta^{vp} = 0.01$ s
$T_o = 295$ K	$a_2 = 20$ GPa	$\ell_2 = 5\ \mu m$	$\eta^{vd} = 0.01$ s
$T_m = 1800$ K	$b_2 = 0.25$ N	$\ell_3 = 0$	$\beta = 0$
$\rho = 7850\ kg/m^3$	$k_2 = 15\ GPa^{-1}$	$\ell_4 = 0$	$m_1 = 0.94$
$c_v = 266$ J/kg K	$l_d = 0$	$\ell_5 = 14\ \mu m$	$m_2 = 0.94$
$c_p = 452$ J/kg K	$a_3 = 0$	$n = 1$	$\phi^c_{eq} = 0.30$
$\gamma = 1.7$	$a_4 = 0$	$\eta_r = 0$	$P_{cutoff} = 160$ GPa
Projectile material of hardened arne tool steel			
$E = 204$ GPa	$\nu = 0.33$	$\rho = 7850\ kg/m^3$	$Y_o = 1900$ MPa
$E_t = 15$ GPa	$\varepsilon_f = 2.15\%$		

width for the three finite element discretizations. Moreover, Figure 4(b) shows that the magnitude and the distribution of the equivalent viscoplastic strain are almost independent of the mesh refinement. It can be seen that as we refine the mesh identical results are obtained.

It is noteworthy that from results not reported here, we observe that with increasing viscosity, the probability at which the results become mesh independent is decreased. Also, for very high viscosity values no localization is observed, but necking behavior is observed. Moreover, as we increase the deformation to very high strain values, we observe initially the development of shear bands, which is followed at a later stage by the evolution of a necking failure mode.

Strip with a Geometrical Imperfection

We notice that in the absence of a physically motivated length-scale, which would govern the width of the shear band, a scale is inherently introduced in the problem by the mesh size when using the finite element method. To remedy the spurious mesh sensitivity of the numerical results, an internal length-scale needs to be incorporated in the continuum description. The following examples demonstrate the potential of the gradient approach (without viscosity and damage) in solving the mesh sensitivity problem in quasi-static problems.

The simulation of a strip with a geometrical imperfection under low impact tensile loading is carried out. The geometric definition of the specimen is depicted in Figure 5. The strip is constrained at the bottom, while a tensile velocity of 20 mm/s is imposed at the top. The constitutive

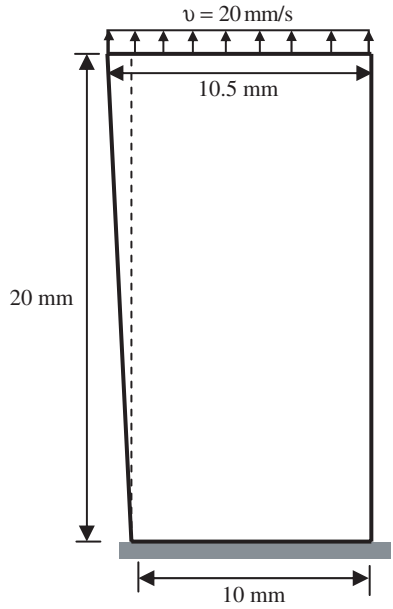

Figure 5. *Problem description of a strip with geometrical imperfection and subjected to low tensile impact velocity.*

parameters used in the computation are listed in Table 2 for the target material (Weldox 460 E steel). Two uniform meshes (mesh 1: 10×20, mesh 2: 20×40) are used with four-noded quadrilateral plane-strain elements. To avoid a homogeneous solution, we slightly increase the width of the specimen toward the top, so that the shear band will be initiated at the bottom left and develops with an inclination angle of 45°.

In Figure 6(a) the deformation patterns for both meshes are plotted for a zero length-scale, $\ell = 0$. We observe that the width of the shear band is determined by the element size. Deformation is localized along a line of integration points. Mesh dependence is also obvious from the effective plastic strain plots in Figure 7(a). When the mesh is refined, the dissipated energy decreases. In Figure 8(a), the overall load–deflection responses are different for the two resolutions. Moreover, it can be shown from these results that the inclusion of the geometrical nonlinearity in the dissipation of the strain softening material cannot solve the discretization dependence.

To solve the mesh-sensitivity problem, a length-scale parameter of 2.5 mm ($\ell = 2.5$ mm) is assumed to keep the field equations well-posed. In Figure 6(b), the deformation patterns are plotted for the two considered meshes. By comparison with the results of Figure 6(a), we observe that the

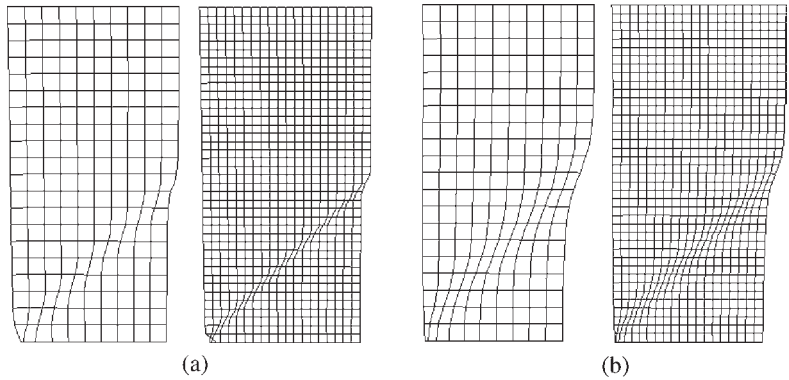

Figure 6. *The deformation patterns for 10×20 and 20×40 meshes: (a) results when $\ell = 0$ and (b) results when $\ell = 2.5$.*

shear band has a finite width, which is almost independent of the finite element size. The inclination of the shear band is close to 45°. Also, a similar distribution of the effective plastic strain contours can be observed in Figure 7(b) for the two meshes, which corroborates the mesh objectivity of results. In Figure 8(b), the overall load–deflection responses is essentially identical for the two resolutions. Apparently, no visible discretization sensitivity is present in the results.

Since the formulation of the gradient dependent theory includes an internal length-scale as a material parameter, numerical solutions employing a strain-softening model are no longer dependent on numerical discretization. However, one limitation to the discretization remains. The width of the localization zone needs to be many times (roughly 6) larger than the element size for proper calculation of the plastic strain.

Projectile Penetrating a Target

The recent advances in aerospace and war capabilities have made necessary the modification of the design of structures so that they can resist penetration and perforation by projectiles with much higher impact energies. In this respect, high performance materials need to be developed so that they can offer significant advantages over the currently used materials. Specific mechanical properties are targeted by the aid of these new materials, such as high specific strength, high stiffness, and low coefficient of thermal expansion. Therefore, the high velocity impacting mechanism needs to be understood properly to be able to design materials of high ballistic resistant response. However, the exact mechanism by which the impacting target materials undergo fracture and ablation is a relatively

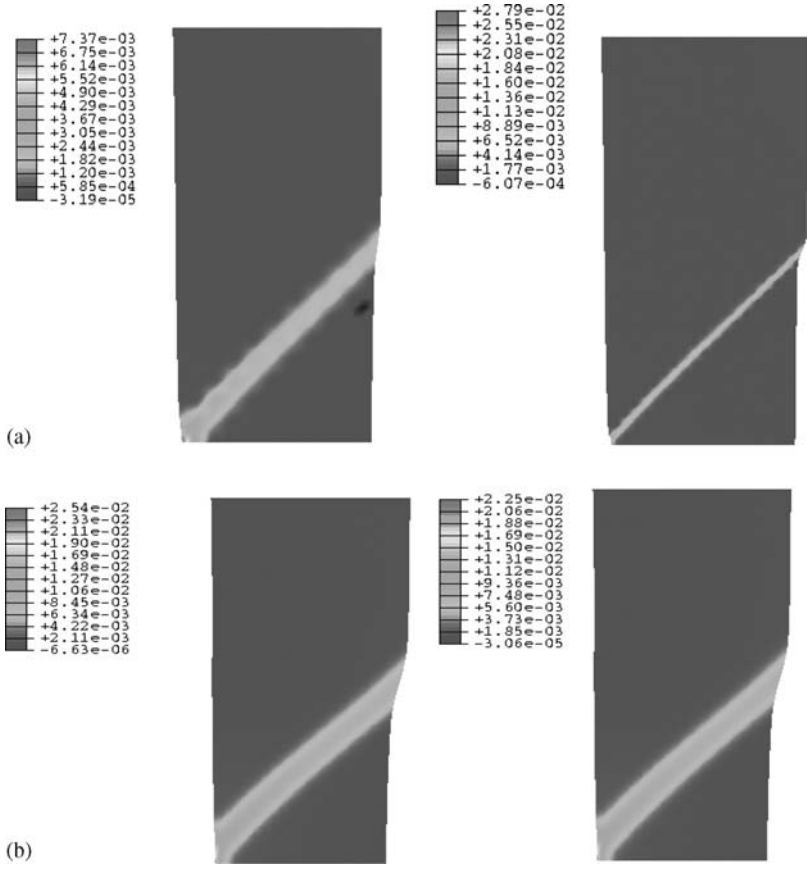

Figure 7. *The effective plastic strain contours for 10×20 and 20×40 meshes: (a) results when $\ell = 0$ and (b) results when $\ell = 2.5$ mm.*

complex process (Zukas, 1990). Generally, strong shock wave–material interactions are generated and propagated along both the projectile and the target, which can lead to fracture at low global inelastic strains. Phenomenologically, as illustrated in Figure 9, the penetration can be viewed as a process to generate a cone-shaped macrocrack in the material, in which, the kinetic energy of the penetrator is dissipated.

The computational model presented in the previous sections is used here to model a blunt projectile impacting a target. This computational model is implemented in ABAQUS/Explicit (2003) using VUMAT user material subroutine. The objective of this numerical example is to investigate if the proposed constitutive equations are able to describe the structural response

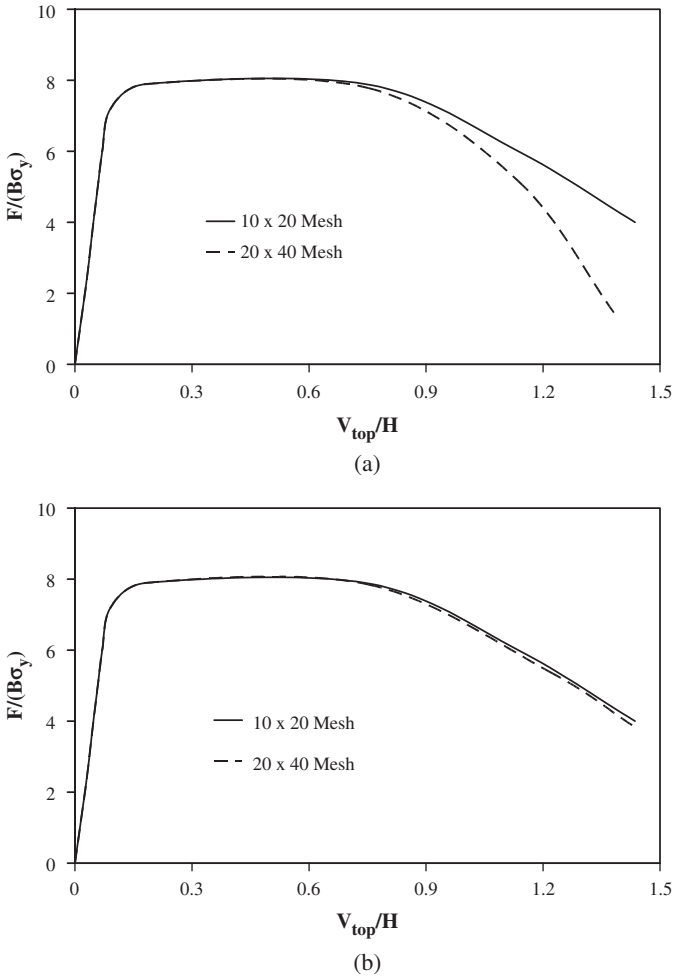

Figure 8. *The load–deflection diagrams for 10 × 20 and 20 × 40 meshes: (a) results when $\ell = 0$ and (b) results when $\ell = 2.5$ mm.*

to projectile impact damage when different failure modes are expected to occur. This is carried out by conducting a numerical simulation of the experimental tests presented by Borvik et al. (2002) for a blunt projectile made of hardened Arne tool steel impacting a circular plate made of Weldox 460 E steel. For more detailed information regarding the numerical scheme, such as the contact-impact algorithm, the automatic mesh generator, the Arbitrary-Lagrangian-Eulerian (ALE) adaptive meshing, and the element

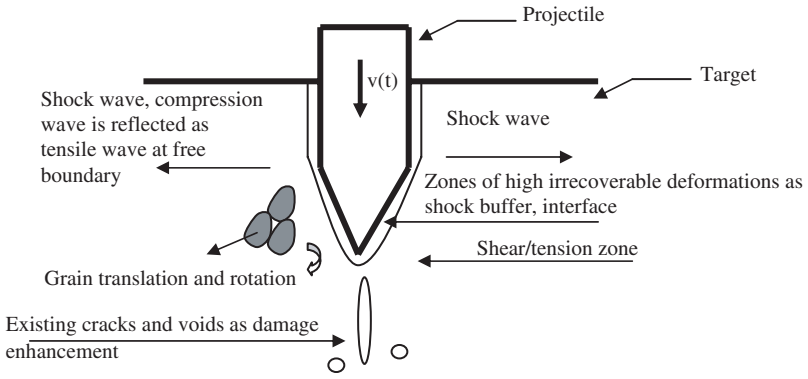

Figure 9. *Phenomenological illustration of the penetration process.*

erosion algorithm, the reader is referred to the manuals of ABAQUS/Explicit (2003).

For simplicity, the projectile is modeled as a bilinear elastic-plastic strain rate-independent von Mises material with isotropic hardening, which is already implemented in ABAQUS/Explicit code. The model material constants of the target material of Weldox 460 E steel and of the projectile material of hardened Arne tool steel are listed in Table 2. These material constants are determined based on the following considerations.

Although there has been tremendous efforts to understand the physical role of the gradient theory, this research area is still in a critical state with controversy. This is to some extent due to the difficulty in calibration of the different material properties associated with the gradient-dependent models, which are impossible to obtain for certain cases. More important is the difficulty of carrying out truly definitive experiments on critical aspects of the evolution of the dislocation, crack, and void structures. Furthermore, the calibration of a gradient-dependent model should not only be based on stress–strain behavior obtained from macroscopic mechanical tests, but should also draw information from micromechanical, gradient-dominant tests, such as micro/nano-indentation tests, microbending tests, and mircotorsion tests. Abu Al-Rub and Voyiadjis (2004) and Voyiadjis and Abu Al-Rub (2005) presented a physically based approach for identification of the material length-scales, ℓ_1 and ℓ_2, from microindentation, microbending, and/or microtorsion tests. Therefore, the values for ℓ_1 and ℓ_2 listed in Table 2 are identified using this approach. The values of ℓ_3 and ℓ_4 are assumed zeros and the value of ℓ_5 is identified based on the one that gives the closest agreement with the experimental results of impact velocity versus the projectile residual velocity. The values for E, ν, T_o, T_m, ρ, c_v, c_p, Υ, η^{vp},

m_1, n, and ϕ_{eq}^{c} are as reported by Borvik et al. (2002). The material constants a_1 and k_1 associated with the plasticity isotropic hardening are identified from a tensile test, while the material constants a_2 and k_2 associated with the plasticity kinematic hardening are identified from a strain control cyclic hardening test (Voyiadjis and Abu Al-Rub, 2003). Damage initiation is assumed to occur at the beginning of loading such that $l_d = 0$. The damage isotropic and kinematic hardening is assumed negligible such that $a_3 = a_4 = 0$ and $h_1 = h_2 = 0$, respectively. The material constants b_1, b_2, and a are identified as $b_1 = (1/2)a_1\ell_1^2$, $b_2 = (1/2)a_2\ell_2^2$, and $a = (1/2)\ell_3^2$. We also assumed that $\eta^{vp} = \eta^{vd}$ and $m_1 = m_2$. The material constants used for the hardened Arne tool steel are as those reported by Borvik et al. (2002). The material constants listed in Table 2 are used to conduct the following simulations.

In these simulations, a four-node two-dimensional axisymmetric element with one integration point and a stiffness based on hourglass control is used. The plot of the initial configuration, showing a part of the target plate and the blunt projectile just prior to impact, is shown in Figure 10. The target plate has a nominal thickness of 12 mm and a diameter of 500 mm, while the nominal length and diameter of the hardened projectile are 80 and 20 mm, respectively. In each run, the target plate is fully clamped at the support, while the projectile is given an initial velocity similar to the one used in the corresponding experiment conducted by Borvik et al. (2002). The initial size of the smallest element in the impact region is $0.25 \times 0.2\,\text{mm}^2$ in all

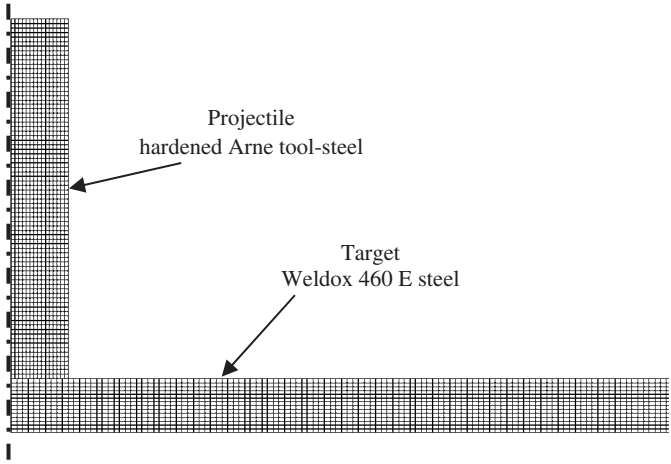

Figure 10. *Finite element mesh plot of the axisymmetric initial configuration just before impact.*

simulations, giving a total of 60 elements over the target thickness. To reduce the computational time, which is affected both by the element size and number, the mesh was somewhat coarsened towards the boundary. Owing to this coarsening, the total number of elements in the target plate is not more than about 10,000 in the simulations. Contact was modeled using an automatic two-dimensional single surface penalty formulation available in ABAQUS/Explicit. Frictional effects are neglected for the blunt projectile. Time increments of order 10^{-8} s are used to satisfy the stability criteria.

An adaptive meshing technique has received the most attention during the last decade to solve high-speed impact damage problems. Coupled ALE is used to extend the domain of application in the Lagrangian codes. The advantages of using adaptive meshing in high-speed impact damage penetration problems are many. It enables the simulation of large inelastic flow in Lagrangian framework. It may also include the possibility to obtain a solution of comparable accuracy using much fewer elements, and hence less computational resources than with a fixed mesh. In addition, it prevents severe mesh distortions and unacceptable small time steps in the simulations. However, the major disadvantage of this method is the possible introduction of inaccuracies and smoothening of the results during mapping of the history variables. Adaptive meshing is used in the following simulations, where 10 adaptive refinements are used in each run.

Borvik et al. (2001) simulations indicate the problem involving shear localization and plugging for blunt projectiles to be mesh size sensitive. However, the numerical solution using the present model is mesh size independent and converges monotonically towards a limit solution when the number of elements over the target thickness becomes sufficiently large. Therefore, the numerical results improve as the element size is reduced until it stabilizes at some value, i.e., the mesh size dependency is not pathological. This is expected since the width of the shear band is known to be in the order of 10–100 μm (Bai and Dodd, 1992).

A direct comparison between the numerical and experimental residual velocity curves for a blunt projectile is shown in Figure 11. As seen, there is good agreement with the experimental results. Moreover, Figure 12 shows that the perforation times obtained from the different numerical simulations are similar and close to the experimental values estimated from high-speed camera images obtained by Borvik et al. (2002). The plots showing perforation of the target plate by a blunt projectile at an impact velocity close to the ballistic limit reported by Borvik et al. (2002) of 210 m/s are shown in Figure 13. Here, the contours of accumulated viscoinelastic strain are plotted on the deformed mesh. It can be seen that limited inelastic deformation occurs outside the localized shear zone. These plots clearly

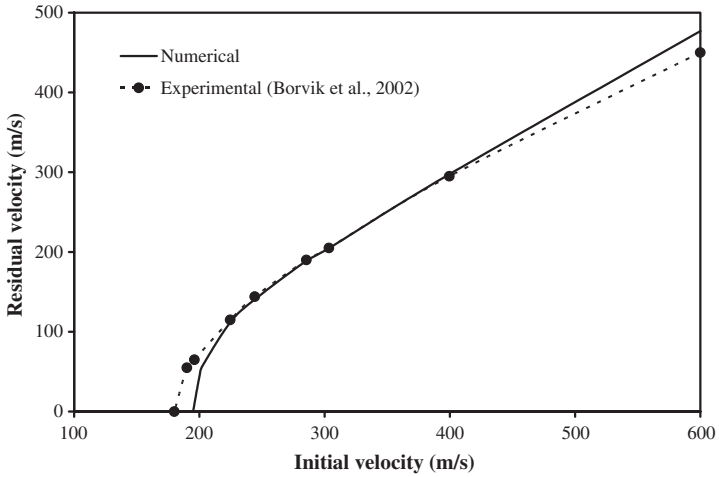

Figure 11. *A comparison between numerical and experimental results for the initial impact velocity vs residual projectile velocity by a blunt projectile.*

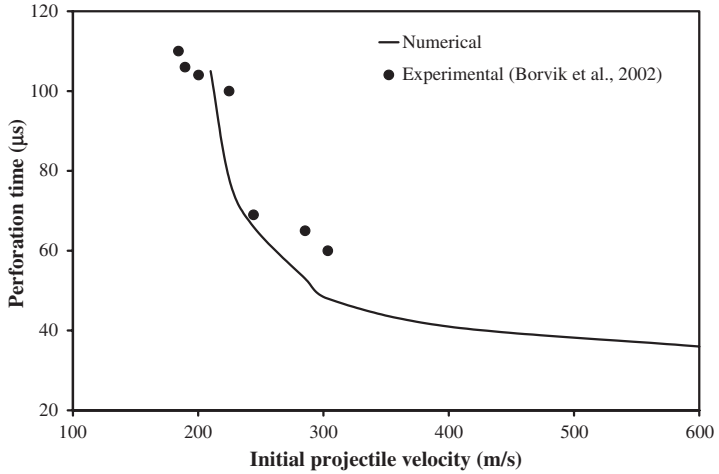

Figure 12. *Comparison between perforation times vs initial impact velocities by a blunt projectile.*

demonstrate that the numerical model qualitatively captures the overall physical behavior of the target during penetration and perforation. Notice also that in these plots, only a part of the complete target plate is shown.

The elements in the impacted area are significantly distorted but stable results are obtained. This delayed the damage evolution process and

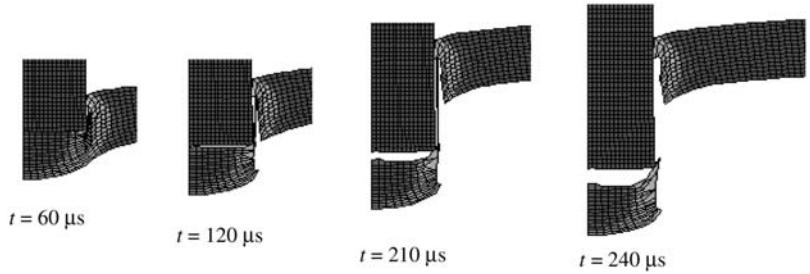

Figure 13. *Perforation of the target plate by a blunt projectile of initial impact velocity of 210 m/s using ALE meshing, plotted as contours of accumulated viscoinelastic strain at different times. The lighter region indicates an accumulated damage between 0.25 and 0.30.*

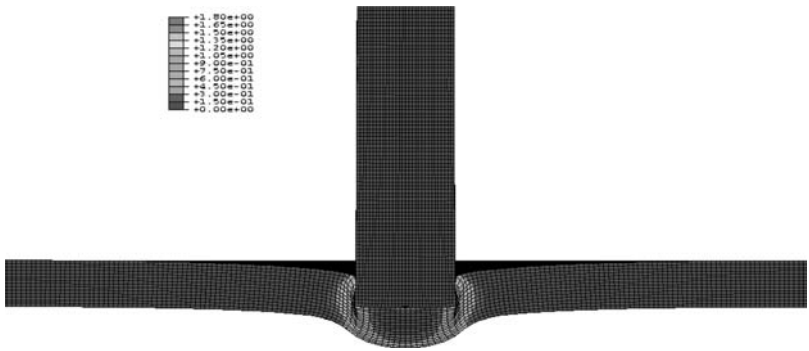

Figure 14. *Penetration of the target plate by a blunt projectile of initial impact velocity of 300 m/s using ALE meshing, plotted as contours of accumulated viscoinelastic strain and showing details of element meshes just after adaptive remeshing.*

consequently the erosion of damaged elements. However, the upper nodes in a critical element do not penetrate the lower nodes, giving a stable solution and no error termination is encountered. Figure 14 shows the element distortion in the target plate just after impact.

The final cross section of a target plate perforated by a blunt projectile at an impact velocity close to the ballistic limit is shown in Figure 15, which is very similar to the experimental cross section obtained by Borvik et al. (2002).

In general, it can be seen that close agreement between the numerical and experimental results is achieved. Hence, the computational methodology presented in this article seems to work well for ductile targets perforated by deformable blunt projectiles. a More elaborate study using the current

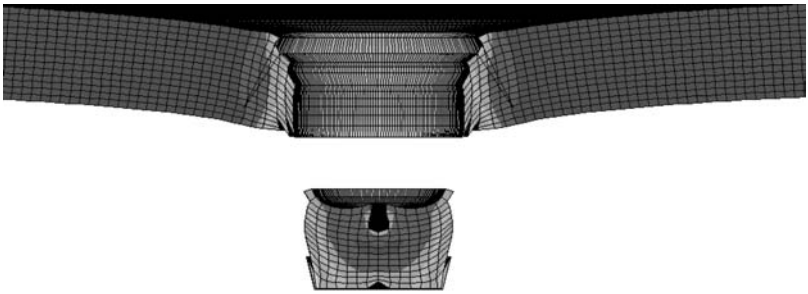

Figure 15. *Final cross section of the target plate perforated by a blunt projectile of initial impact velocity of 300 m/s using ALE meshing and plotted as contours of accumulated viscoinelastic strain. The lighter region part indicates an accumulated damage between 0.25 and 0.30 (critical value).*

gradient-dependent viscoplastic and viscodamage model is needed for simulating high-speed impacts of different target thicknesses and also using different projectile nose shapes (e.g., hemispherical and conical). This is not the subject of this article but will be presented in detail in a forthcoming article by the current authors.

CONCLUSIONS

In the first part of this study, it was recognized that the initiation and propagation of the microdefects depend on both the amplitude and distribution of the inelastic strains/stress in the vicinity around the micro-defect. It means that evolution of the material inelasticity is practically a nonlocal process. These observations imply that there is a need for such a micro-mechanical approach that incorporates material length-scale parameters into the classical constitutive relations. The incorporation of spatial higher-order gradient terms allows us to introduce a 'missing' length-scale into the classical continuum theories allowing the size effect to be captured.

A gradient-enhanced (nonlocal) coupled rate-dependent plasticity and damage model is developed on the continuum level to bridge the gap between the micromechanical and classical continuum inelasticity. The thermodynamical consistency of the gradient-dependent plasticity/damage constitutive relations is discussed thoroughly in Part I of the companion article of this work. Implicit and explicit incorporation of material length-scales is achieved through the development of coupled viscoinelasticity (rate-dependent plasticity/damage) and nonlocal gradient-dependent constitutive

relations, respectively. Therefore, the resulting model incorporates in a very modular fashion the damage and plasticity effects in solids, and most importantly in a highly physically motivated way.

Several numerical algorithms are developed in this part of the article, to integrate the highly nonlinear differential equations effectively and to optimize the computational performance. We have presented a return mapping algorithm for the integration of the proposed model in Part I, sharing remarkably the exact same structure as the classical return mapping employed in the integration of rate-independent plasticity/damage and gradient-independent plasticity/damage. An operator split structure consisting of a trial state followed by the return map is developed by imposing a generalized (rate-independent to rate-dependent) viscoplastic and viscodamage consistency conditions simultaneously. This allows us to integrate both rate-dependent and rate-independent models in a similar fashion. Moreover, a simple and direct computational algorithm is also used for calculation of the Laplacian gradients allowing us to integrate both the gradient-dependent and gradient-independent models in a similar way. Furthermore, a trivially incrementally objective integration scheme is proposed. The proposed finite deformation scheme is based on hypoelastic stress–strain representations and the proposed hypoelastic predictor and coupled viscoplastic–viscodamage corrector algorithm that allows for total uncoupling of the geometrical and material nonlinearities. The nonlinear algebraic system of equations is solved by consistent linearization and the use of the Newton–Raphson iteration. The numerical implementation then involves a series of coupled routines providing the stresses and updates of the corresponding internal variables.

The proposed model and numerical integration algorithms are implemented in the well-known explicit finite element code ABAQUS/Explicit using the material subroutine VUMAT. The first and second numerical simulations presented herein illustrate the numerical performance of the proposed numerical algorithms. They also showed that the proposed model introduces properly the localization limiting of rate-dependent and nonlocal continua: the results of finite element simulations are almost insensitive to mesh refinement, since the width of the shear bands (fracture process zone) is determined by the internal length-scale incorporated in the proposed model.

Moreover, we have presented in this article the application of the proposed model to the numerical simulation of localization and formation of shear bands in structures subjected to high-speed impact loading conditions. Good agreement is obtained between the numerical simulations and experimental results. Therefore, the material length-scale has the potential to predict the size effects in material failure.

We believe that the aforementioned advantages provided by the proposed model do lead to an improvement in the modeling and numerical simulation of high velocity impact related problems. We plan to explore this model further. The study of strain localization and its regularization on impact damage related problems needs further attention to allow us to properly simulate impact damage problems without conducting extensive experiments.

ACKNOWLEDGMENTS

We are indebted to Professor Anthony N. Palazotto for the helpful discussions through the different stages of this work. Financial support for this research has been provided by the AFSOR through the Air Force Institute of Technology at WPAFB, Ohio, under grant number F33601-01-P-0343. This support is gratefully acknowledged. We also acknowledge the financial support under grant number M67854-03-M-6040 provided by the Marine Corps Systems Command, AFSS PGD, Quantico, Virginia. We thankfully acknowledge our appreciation to Howard 'Skip' Bayes, Project Director.

APPENDIX A

From the heat balance equation we have

$$Q_1^{\mathrm{tp}} = \frac{1}{\rho_0 c_{\mathrm{p}}}\left[(\Upsilon\boldsymbol{\tau}' + J^{\mathrm{e}}P\mathbf{1} + T_i\boldsymbol{\beta}) : \frac{\partial f}{\partial \boldsymbol{\tau}} + \left(\frac{V_3}{1-\hat{r}} + \frac{V_7\nabla^2 r}{(1-\hat{r})^2}\right)\left(1 - k_1\bar{\hat{\boldsymbol{R}}}\right) - \frac{k_1 V_7}{1-\hat{r}}\nabla^2\bar{\boldsymbol{R}} - \left(\boldsymbol{V}_4 : \hat{\boldsymbol{M}} + V_8 : \nabla^2\hat{\boldsymbol{M}}\right) : \left(\frac{\partial f}{\partial \bar{\boldsymbol{X}}} + k_2\bar{\hat{\boldsymbol{X}}}\right) - k_2\boldsymbol{V}_8 : \hat{\boldsymbol{M}} : \nabla^2\bar{\boldsymbol{X}}\right] \tag{A-1}$$

$$Q_2^{\mathrm{tp}} = \frac{1}{\rho_{\mathrm{o}} c_{\mathrm{p}}}\left[\frac{V_7}{1-\hat{r}}\left(1 - k_1\bar{\hat{\boldsymbol{R}}}\right) - \boldsymbol{V}_8 : \hat{\boldsymbol{M}} : \left(\frac{\partial f}{\partial \bar{\boldsymbol{X}}} + k_2\bar{\hat{\boldsymbol{X}}}\right)\right] \tag{A-2}$$

$$Q_1^{\mathrm{td}} = \frac{1}{\rho_{\mathrm{o}} c_{\mathrm{p}}}\left[(\Upsilon\boldsymbol{\tau}' + J^{\mathrm{e}}P\mathbf{1} + T_i\boldsymbol{\beta}) : \frac{\partial g}{\partial \boldsymbol{\tau}} + V_5\left(1 - h_1\hat{K}\right) - h_1 V_9\nabla^2 K - \boldsymbol{V}_6 : \left(\frac{\partial g}{\partial \boldsymbol{H}} + h_2\hat{\boldsymbol{H}}\right) - h_2\boldsymbol{V}_{10} : \nabla^2\boldsymbol{H}\right] \tag{A-3}$$

$$Q_2^{\mathrm{td}} = \frac{1}{\rho_{\mathrm{o}} c_{\mathrm{p}}}\left[V_9\left(1 - h_1\hat{K}\right) - \boldsymbol{V}_{10}\left(\frac{\partial g}{\partial \boldsymbol{H}} + h_2\hat{\boldsymbol{H}}\right)\right] \tag{A-4}$$

From the viscoplasticity generalized consistency condition we obtain

$$\boldsymbol{Z}^p = -\left(\frac{\partial f}{\partial T} - \frac{\partial f}{\partial \boldsymbol{\tau}} : \boldsymbol{\beta}\right) \cdot (J^{\mathrm{e}} P\mathbf{1} + T\boldsymbol{\beta}) \tag{A-5}$$

$$\begin{aligned} Q_1^p = Q_1^{\mathrm{tp}} &- \frac{\partial f}{\partial \boldsymbol{\tau}} : \left(\boldsymbol{C} : \frac{\partial f}{\partial \boldsymbol{\tau}} + \boldsymbol{A} : \frac{\partial f}{\partial \boldsymbol{Y}}\right) + \left[\frac{\partial f}{\partial p} + \frac{1}{\Delta t}\frac{\partial f}{\partial \dot{p}}\right] \frac{\left(1 - k_1 \bar{\widehat{\boldsymbol{R}}}\right)}{1 - \widehat{r}} \\ &+ \left[\frac{\partial f}{\partial \nabla^2 p} + \frac{1}{\Delta t}\frac{\partial f}{\partial \nabla^2 \dot{p}}\right] \times \left[\frac{\nabla^2 r}{(1 - \widehat{r})^2}\left(1 - k_1 \bar{\widehat{\boldsymbol{R}}}\right) - \frac{k_1}{1 - \widehat{r}} \nabla^2 \bar{\widehat{\boldsymbol{R}}}\right] \\ &- \frac{\partial f}{\partial \boldsymbol{\alpha}} : \widehat{\boldsymbol{M}} : \left(\frac{\partial f}{\partial \bar{\widehat{\boldsymbol{X}}}} + k_2 \bar{\widehat{\boldsymbol{X}}}\right) - \frac{\partial f}{\partial \nabla^2 \boldsymbol{\alpha}} : \left[\nabla^2 \widehat{\boldsymbol{M}} : \left(\frac{\partial f}{\partial \bar{\widehat{\boldsymbol{X}}}} + k_2 \bar{\widehat{\boldsymbol{X}}}\right) + k_2 \widehat{\boldsymbol{M}} : \nabla^2 \bar{\widehat{\boldsymbol{X}}}\right] \\ &+ \frac{\partial f}{\partial \boldsymbol{\phi}} : \frac{\partial f}{\partial \boldsymbol{Y}} \end{aligned} \tag{A-6}$$

$$\begin{aligned} Q_2^p = Q_2^{\mathrm{tp}} &- a \frac{\partial f}{\partial \boldsymbol{\tau}} : \boldsymbol{A} : \frac{\partial f}{\partial \boldsymbol{Y}} + \left[\frac{\partial f}{\partial \nabla^2 p} + \frac{1}{\Delta t}\frac{\partial f}{\partial \nabla^2 \dot{p}}\right] \frac{\left(1 - k_1 \bar{\widehat{\boldsymbol{R}}}\right)}{1 - \widehat{r}} \\ &- \frac{\partial f}{\partial \nabla^2 \boldsymbol{\alpha}} : \widehat{\boldsymbol{M}} : \left(\frac{\partial f}{\partial \bar{\widehat{\boldsymbol{X}}}} + k_2 \bar{\widehat{\boldsymbol{X}}}\right) + \frac{\partial f}{\partial \nabla^2 \boldsymbol{\phi}} : \frac{\partial f}{\partial \boldsymbol{Y}} \end{aligned} \tag{A-7}$$

$$Q_3^p = Q_1^{\mathrm{td}} - \frac{\partial f}{\partial \boldsymbol{\tau}} : \left(\boldsymbol{C} : \frac{\partial g}{\partial \boldsymbol{\tau}} + \boldsymbol{A} : \frac{\partial g}{\partial \boldsymbol{Y}}\right) + \frac{\partial f}{\partial \boldsymbol{\phi}} : \frac{\partial g}{\partial \boldsymbol{Y}} \tag{A-8}$$

$$Q_4^p = Q_2^{\mathrm{td}} - a \frac{\partial f}{\partial \boldsymbol{\tau}} : \boldsymbol{A} : \frac{\partial g}{\partial \boldsymbol{Y}} + \frac{\partial f}{\partial \nabla^2 \boldsymbol{\phi}} : \frac{\partial g}{\partial \boldsymbol{Y}} \tag{A-9}$$

From the viscodamage generalized consistency condition we have

$$\boldsymbol{Z}^d = -\left(\frac{\partial g}{\partial T} - \frac{\partial g}{\partial \boldsymbol{\tau}} : \boldsymbol{\beta}\right) \cdot (J^{\mathrm{e}} P\mathbf{1} + T\boldsymbol{\beta}) \tag{A-10}$$

$$Q_1^d = Q_1^{\mathrm{tp}} - \frac{\partial g}{\partial \boldsymbol{\tau}} : \left(\boldsymbol{C} : \frac{\partial f}{\partial \boldsymbol{\tau}} + \boldsymbol{A} : \frac{\partial f}{\partial \boldsymbol{Y}}\right) + \frac{\partial g}{\partial \boldsymbol{\phi}} : \frac{\partial f}{\partial \boldsymbol{Y}} \tag{A-11}$$

$$Q_2^d = Q_2^{\mathrm{tp}} - a \frac{\partial g}{\partial \boldsymbol{\tau}} : \boldsymbol{A} : \frac{\partial f}{\partial \boldsymbol{Y}} + \frac{\partial g}{\partial \nabla^2 \boldsymbol{\phi}} : \frac{\partial f}{\partial \boldsymbol{Y}} \tag{A-12}$$

$$Q_3^d = Q_1^{\text{td}} - \frac{\partial g}{\partial \boldsymbol{\tau}} : \left(\boldsymbol{C} : \frac{\partial g}{\partial \boldsymbol{\tau}} + \boldsymbol{A} : \frac{\partial g}{\partial \boldsymbol{Y}} \right) + \frac{\partial g}{\partial r}\left(1 - h_1 \widehat{K}\right) - h_1 \frac{\partial g}{\partial \nabla^2 r} \nabla^2 K + \frac{1}{\Delta t} \frac{\partial g}{\partial \dot{r}}$$
$$- \frac{\partial g}{\partial \boldsymbol{\Gamma}} : \left(\frac{\partial g}{\partial \boldsymbol{H}} + h_2 \widehat{\boldsymbol{H}} \right) - h_2 \frac{\partial g}{\partial \nabla^2 \boldsymbol{\Gamma}} : \nabla^2 \boldsymbol{H} + \frac{\partial g}{\partial \boldsymbol{\phi}} : \frac{\partial g}{\partial \boldsymbol{Y}} \tag{A-13}$$

$$Q_4^d = Q_2^{\text{td}} - a \frac{\partial g}{\partial \boldsymbol{\tau}}\bigg|^T \boldsymbol{A} \frac{\partial g}{\partial \boldsymbol{Y}} + \frac{\partial g}{\partial \nabla^2 r}\left(1 - h_1 \widehat{K}\right)$$
$$+ \frac{1}{\Delta t} \frac{\partial g}{\partial \nabla^2 \dot{r}} - \frac{\partial g}{\partial \nabla^2 \boldsymbol{\Gamma}} \left(\frac{\partial g}{\partial \boldsymbol{H}} + h_2 \widehat{\boldsymbol{H}} \right) + \frac{\partial g}{\partial \nabla^2 \boldsymbol{\phi}}\bigg|^T \frac{\partial g}{\partial \boldsymbol{Y}} \tag{A-14}$$

REFERENCES

ABAQUS (2003). User Manual, Version 6.3, Habbitt, Karlsson and Sorensen, Inc., Providence, RI.

Abu Al-Rub, R.K. and Voyiadjis, G.Z. (2004). Analytical and Experimental Determination of the Material Intrinsic Length Scale of Strain Gradient Plasticity Theory from Micro- and Nano-Indentation Experiments, *International Journal of Plasticity*, **20**(6): 1139–1182.

Abu Al-Rub, R.K. and Voyiadjis, G.Z. (2005). A Direct Finite Element Implementation of the Gradient Plasticity Theory, *International Journal for Numerical Methods in Engineering*, **63**(4): 603–629.

Bai, Y. and Dodd, B. (1992). *Adiabatic Shear Localization: Occurrence, Theories and Applications*, Pergamon Press, Oxford.

Borvik, T., Hopperstad, O.S., Berstad, T. and Langseth, M. (2001). Numerical Simulation of Plugging Failure in Ballistic Penetration, *Int. J. Solids Structures*, **38**: 6241–6264.

Borvik, T., Langseth, M., Hopperstad, O.S. and Malo, K.A. (2002). Perforation of 12 mm Thick Steel Plates by 20 mm Diameter Projectiles with Flat, Hemispherical and Conical Noses – Part I: Experimental Study, *International Journal of Impact Engineering*, **27**(1): 19–35.

Chen, J. and Yuan, H. (2002). A Micro-Mechanical Damage Model Based on Gradient Plasticity: Algorithms and Applications, *Int. J. Numer. Meth. Engng.*, **54**: 399–420.

Comi, C. and Perego, U. (1996). A Generalized Variable Formulation for Gradient Dependent Softening Plasticity, *Int. J. Numer. Meth. Engng.*, **39**: 3731–3755.

de Borst, R. and Mühlhaus, H.-B. (1992). Gradient-Dependent Plasticity Formulation and Algorithmic Aspects, *Int. J. Numer. Methods Engrg.*, **35**: 521–539.

de Borst, R. and Pamin, J. (1996). Some Novel Developments in Finite Element Procedures for Gradient Dependent Plasticity, *Int. J. Numer. Methods Engrg.*, **39**: 2477–2505.

de Borst, R., Pamin, J. and Geers, M. (1999). On Coupled Gradient-Dependent Plastcity and Damage Theories with a View to Localization, *Eur. J. Mech. A/Solids*, **18**: 939–962.

de Borst, R., Sluys, L.J., Mühlhaus, H.-B. and Pamin, J. (1993). Fundamental Issues in Finite Element Analysis of Localization of Deformation, *Engineering Computations*, **10**: 99–121.

Liebe, T., Menzel, A. and Steinmann, P. (2003). Theory and Numerics of Geometrically Nonlinear Gradient Plasticity, *Int. J. Eng. Sci.*, **41**: 1603–1629.

Matsushima, T., Chambon, R. and Caillerie, D. (2002). Large Strain Finite Element Analysis of a Local Second Gradient Model: Application to Localization, *Int. J. Numer. Meth. Engng.*, **54**: 499–521.

Mikkelsen, L.P. (1997). Post-Necking Behavior Modeling by a Gradient Dependent Plasticity Theory, *Int. J. Solids Structures*, **34**: 4531–4546.

Nedjar, B. (2001). Elastoplastic-Damage Modeling Including the Gradient of Damage: Formulation and Computational Aspects, *Int. J. Solids Struct.*, **38**: 5421–5451.

Pamin, J. (1994). Gradient-Dependent Plasticity in Numerical Simulation of Localization Phenomena, Dissertation, Delft University of Technology.

Pamin, J., Askes, H. and de Borst, R. (2003). Two Gradient Plasticity Theories Discretized with the Element-Free Galerkin Method, *Comput. Methods Appl. Mech. Engrg.*, **192**: 2377–2403.

Peerlings, R.H.J., de Borst, R., Brekelmans, W.A.M. and de Vree, J.H.P. (1996). Gradient Enhanced Damage for Quasi-Brittle Materials, *Int. J. Numer. Methods in Engrg.*, Wiley, London, **39**: 3391–3403.

Ramaswamy, S. and Aravas, N. (1998a). Finite Element Implementation of Gradient Plasticity Models. Part I: Gradient-Dependent Yield Functions, *Comput. Methods Appl. Mech. Engrg.*, **163**: 11–32.

Ramaswamy, S. and Aravas, N. (1998b). Finite Element Implementation of Gradient Plasticity Models. Part II: Gradient-Dependent Evolution Equations, *Comput. Methods Appl. Mech. Engrg.*, **163**: 33–53.

Simo, J.C. and Hughes, T.J.R. (1998). Computational Inelasticity, In: *Interdisciplinary Applied Mathematics*, Springer, New York.

Svedberg, T. and Runesson, K. (2000). An Adaptive Finite Element Algorithm for Gradient Theory of Plasticity with Coupling to Damage, *Int. J. of Solids and Structures*, **37**: 7481–7499.

Voyiadjis, G.Z. and Abu Al-Rub, R.K. (2003). Thermodynamic Based Model for the Evolution Equation of the Backstress in Cyclic Plasticity, *International Journal of Plasticity*, **19**(12): 2121–2147.

Voyiadjis, G.Z. and Abu Al-Rub, R.K. (2005). Gradient Plasticity Theory with a Variable Length Scale Parameter, *International Journal of Solids and Structures*, **42**(14): 3998–4029.

Voyiadjis, G.Z., Abu Al-Rub, R.K. and Palazotto, A.N. (2003). Non-Local Coupling of Viscoplasticity and Anisotropic Viscodamage for Impact Problems Using the Gradient Theory, *Archives of Mechanics*, **55**: 39–89.

Voyiadjis, G.Z., Abu Al-Rub, R.K. and Palazotto, A.N. (2004). Thermodynamic Formulations for Non-Local Coupling of Viscoplasticity and Anisotropic Viscodamage for Dynamic Localization Problems Using Gradient Theory, *International Journal of Plasticity*, **20**: 981–1038.

Voyiadjis, G.Z., Deliktas, B. and Aifantis, E.C. (2001). Multiscale Analysis of Multiple Damage Mechanics Coupled with Inelastic Behavior of Composite Materials, *Journal of Engineering Mechanics*, **127**(7): 636–645.

Zervos, A., Papanastasious, P. and Vardoulakis, I. (2001). A Finite Element Displacement Formulation for Gradient Elastoplasticity, *Int. J. Numer. Meth. Engng.*, **50**: 1369–1388.

Zhu, Y.Y. and Cescetto, S. (1995). Fully Coupled Elasto-Visco-Plastic Damage Theory for Anisotropic Materials, *Int. J. Solids Structures*, **32**: 1607–1641.

Zukas, J.A. (ed.) (1990). *High Velocity Impact Dynamics*, John Wiley & Sons, Inc., New York.